

Winter 1994

On the occurrence of solar flares observed with the Burst and Transient Source experiment

Douglas Alan Biesecker
University of New Hampshire, Durham

Follow this and additional works at: <https://scholars.unh.edu/dissertation>

Recommended Citation

Biesecker, Douglas Alan, "On the occurrence of solar flares observed with the Burst and Transient Source experiment" (1994).
Doctoral Dissertations. 1815.
<https://scholars.unh.edu/dissertation/1815>

This Dissertation is brought to you for free and open access by the Student Scholarship at University of New Hampshire Scholars' Repository. It has been accepted for inclusion in Doctoral Dissertations by an authorized administrator of University of New Hampshire Scholars' Repository. For more information, please contact nicole.hentz@unh.edu.

INFORMATION TO USERS

This manuscript has been reproduced from the microfilm master. UMI films the text directly from the original or copy submitted. Thus, some thesis and dissertation copies are in typewriter face, while others may be from any type of computer printer.

The quality of this reproduction is dependent upon the quality of the copy submitted. Broken or indistinct print, colored or poor quality illustrations and photographs, print bleedthrough, substandard margins, and improper alignment can adversely affect reproduction.

In the unlikely event that the author did not send UMI a complete manuscript and there are missing pages, these will be noted. Also, if unauthorized copyright material had to be removed, a note will indicate the deletion.

Oversize materials (e.g., maps, drawings, charts) are reproduced by sectioning the original, beginning at the upper left-hand corner and continuing from left to right in equal sections with small overlaps. Each original is also photographed in one exposure and is included in reduced form at the back of the book.

Photographs included in the original manuscript have been reproduced xerographically in this copy. Higher quality 6" x 9" black and white photographic prints are available for any photographs or illustrations appearing in this copy for an additional charge. Contact UMI directly to order.

UMI

University Microfilms International
A Bell & Howell Information Company
300 North Zeeb Road, Ann Arbor, MI 48106-1346 USA
313/761-4700 800/521-0600

.

Order Number 9518480

**On the occurrence of solar flares observed with the Burst and
Transient Source experiment**

Biesecker, Douglas Alan, Ph.D.

University of New Hampshire, 1994

U·M·I
300 N. Zeeb Rd.
Ann Arbor, MI 48106

ON THE OCCURRENCE OF SOLAR FLARES
OBSERVED WITH
THE BURST AND TRANSIENT SOURCE EXPERIMENT

BY

DOUGLAS ALAN BIESECKER

B.S., Physics, Carnegie Mellon University, 1987

M.S., Physics, University of New Hampshire, 1991

DISSERTATION

Submitted to the University of New Hampshire

in Partial Fulfillment of

the Requirements for the Degree of

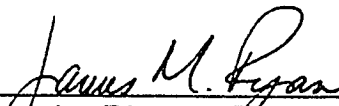
Doctor of Philosophy

in

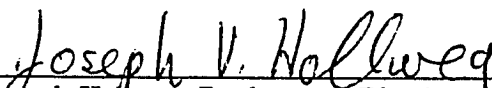
Physics

December, 1994

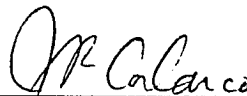
This dissertation has been examined and approved.



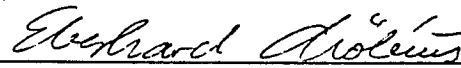
Dissertation Director, James Ryan
Associate Professor of Physics and Earth, Oceans, and
Space



Joseph Hollweg, Professor of Physics and Earth, Oceans,
and Space




John Calarco, Professor of Physics



Eberhard Möbius, Associate Professor of Physics and
Earth, Oceans, and Space



David Forrest, Research Associate Professor of Physics
and Earth, Oceans, and Space



Brian Dennis, Astrophysicist, Laboratory for Astronomy
and Solar Physics, Solar Physics Branch, NASA

December 2, 1994
Date

This dissertation is dedicated to the Solar Maximum Mission:
the team members who made me realize it was possible;
the spacecraft, whose in-flight repair still inspires me.

ACKNOWLEDGEMENTS

I wish to give my most sincere thanks to my research advisor, Dr. James Ryan for the guidance, encouragement, and support he has given me over the years this project took to complete. This dissertation would have been impossible without his help.

I am grateful to Drs. Joseph Hollweg, Eberhard Möbius, David Forrest, John Calarco and Brian Dennis for their help as members of my Ph.D. committee and for what they have taught me about the Sun, the stars, and the instruments used to look at them.

For the help they have given me throughout the course of my research I want to thank Drs. Alanna Connors, Dan Morris, and Richard Schwartz and R. Marc Kippen, C. Alex Young and John Macri.

I also want to thank Drs. Chryssa Kouveliotou and Upendra Desai for getting me started in the field of solar physics.

I am especially grateful for the immense amount of computer and \TeX help that Dr. Tom Milliman gave me and also to Neil Schonwald who answered far too many computer questions.

Debbie Watson and Emily Leviness deserve a special thank you for the incredible help they gave me finding references that Sherlock Holmes would have had difficulty discovering.

I am very thankful to Ben Hersh, Bonnie Kwiatkowski, and Doug Larson for making graduate school bearable and to Cheenu Kappadath for making graduate school fun.

I want to thank Dot Kittredge, Pat Frost, Nancy DeSchuiteneer, and Naomi Preble for their help with more paperwork than I ever care to see again.

Karol LaCroix, the Interim Dean of the Graduate School, and Harry Richards, Associate Dean of the Graduate School deserve my thanks for listening to my griping and for pushing me to finish.

I must also thank Jody Berman, Bruce Carle, and the Graduate Student Organization for letting me vent my frustrations at the university administration.

I want to thank my parents who taught me the importance of education and who have encouraged me in my many years of study.

Finally, I reserve my deepest thanks for my wife, Kelly Eaton Biesecker, who has had to endure living with me, a nearly impossible task. It is her devotion which made completing this dissertation possible.

TABLE OF CONTENTS

DEDICATION	iii
ACKNOWLEDGEMENTS	iv
LIST OF TABLES	ix
LIST OF FIGURES	x
ABSTRACT	xiv

CHAPTER	PAGE
I. INTRODUCTION	1
Importance of Studying the Sun	1
Solar Flares and Microflares	1
Using BATSE to Observe Solar Flares	3
II. THE SUN	5
The Interior	5
The Atmosphere	7
Magnetic Fields	8
III. SOLAR FLARES	10
General Flare Picture	10
Microflares	11
IV. THE EXPERIMENT	16
Instrumentation	16
Compton Gamma Ray Observatory	16
Burst and Transient Source Experiment	16
Data Processing	18
Flare Search	18

	Source Location.....	23
	Detector correction.....	24
	Trigger identification.....	25
V.	ANALYSIS AND RESULTS.....	28
	Flare Frequency Distributions.....	28
	Differential Distribution of Flare Peak Rates.....	28
	All data.....	28
	Search sensitivity.....	29
	Best data selection.....	32
	Variations in Differential Distribution.....	33
	Data selection.....	33
	Phase of 51 day period.....	34
	Variations with activity.....	36
	Trend over experiment duration.....	38
	Time Series Analyses.....	39
	Autocorrelation of the Flare Frequency.....	40
	Wavelet Analysis of the Flare Frequency.....	43
	Time Distribution of Solar Flares.....	47
	Randomness of flare occurrence.....	48
	Flare size dependence.....	53
VI.	DISCUSSION.....	55
	Coronal Heating.....	55
	Deviations From a Power-law Distribution.....	63
	Avalanche Model of Solar Flares.....	64
	Avalanche Model Predictions.....	66
	Power-law index.....	66
	Random occurrence of flares.....	67

Stochastic Flare Model.....	68
Sympathetic Flares.....	70
Solar Periods.....	73
Complexes of Activity 'Hot Spots'.....	75
VII. CONCLUSIONS.....	77
LIST OF REFERENCES.....	81

LIST OF TABLES

Table 6.1	Solar flare size frequency distributions	58
Table 6.2	Flare size frequency distributions for stellar sources	62

LIST OF FIGURES

Fig. 2.1	The overall structure of the Sun, indicating the sizes of the various regions and their temperatures (in degrees K) and densities (in kg m^{-3}). The thicknesses of the photosphere and chromosphere are not to scale	6
Fig. 2.2	An illustrative model for the variation of the temperature with height in the solar atmosphere	7
Fig. 2.3	The structure of a magnetohydrostatic network model. Temperature contours between $\log T = 6.1$ and $\log T = 5.4$ are marked	9
Figs. 3.1a-d	BATSE energy channel 1 light curves. These four events are considered microflares in this work	12
Figs. 3.1e-h	BATSE energy channel 1 light curves. These four events are examples of flares that could be constructed from a superposition of microflares	12
Fig. 3.2	The distribution of the integral rate of occurrence of events vs. peak 20 keV photon flux for the solar hard X-ray microflares observed in this balloon flight. Also shown for comparison is the distribution of solar flare hard X-ray bursts reported by Datlowe, Elcan, and Hudson	14
Fig. 4.1	The location of the BATSE instrument on the Compton Gamma Ray Observatory and the spacecraft coordinate system	17
Fig. 4.2a	A cut-away view of a BATSE detector module	17
Fig. 4.2b	An illustration of the BATSE detector aspect. The faces of the modules are parallel to the sides of a regular octahedron	17
Fig. 4.3	The solar viewing duty cycle is plotted for the truncated julian dates 8387 through 8777	18
Fig. 4.4	A sample BATSE light curve available from the Solar Data Analysis Center. The data from one spacecraft orbit are shown. The 8 scaled light curves are, from top to bottom, the first energy channel of the four solar facing detectors, the summed solar facing detectors first two energy channels, the summed solar facing charged particle detectors, and the summed non-solar facing detectors first energy channel	19

Fig. 4.5	A sample of the raw BATSE data, its second difference, and second difference of smoothed data are shown. The top light curve is the BATSE count rate for the first energy channel of the most solar-facing detector. The middle curve is the second difference of the count rate divided by the standard deviation of the second difference. The bottom curve is W (Eq. 4.7), for $M = 8$ and $Z = 4$	22
Fig. 4.6	The second difference coefficients C_{ij} are shown for the cases where $Z = 0, 1, 2, 3,$ and 4 . The $Z = 0$ case is described by Eq. 4.3. The coefficients for $Z > 0$ are higher order smoothing cases. The $Z = 4$ case is generally used for this work	23
Fig. 4.7	The weighted average of the normalized count rates in the solar-facing detectors. A value of 1.0 identifies events that are consistent with the solar direction	26
Fig. 4.8a	The weighted average of the normalized count rates in the solar-facing detectors. A value of 1.0 indicates events that are consistent with the solar direction. The triggers were detected when the spacecraft was in the earth's shadow	27
Fig. 4.8b	The weighted average of the normalized count rates in the solar-facing detectors. A value of 1.0 indicates events that are consistent with the solar direction. The triggers were detected on the day side of the earth	27
Fig. 5.1	The differential frequency distribution of BATSE flare peak rates. The peak rates are normalized to a detector with normal incidence	29
Fig. 5.2a	The turnover in the differential distribution of flare peak rates as a function of flare background rate. The solid line is a best fit to the data. The arrows indicate the ideal limit observable with BATSE	30
Fig. 5.2b	The turnover in the differential distribution of flare peak rates as a function of solar viewing angle. The solid line is a best fit to the data. The arrow indicates the ideal limit for a detector with normal incidence to the sun	30
Fig. 5.3	Flares detected with search algorithm as a function of the flare background rate. The contours indicate the density of flares. The dashed-line indicates the peak rate equivalent to a $3\sqrt{N_b}$ detection, illustrating the sensitivity of the search algorithm ...	31
Fig. 5.4	The differential frequency distribution of BATSE flare peak rates for the case where the background rate is $\leq 1250 \text{ s}^{-1}$ and $\cos\theta \geq 0.90$. The peak rates are normalized to a detector with normal incidence	32

Fig. 5.5	The 51 day epoch-folded daily flare rate. Filled squares indicate the peak of the 51 day phase, open circles indicate the minimum of the phase	35
Fig. 5.6	Differential distribution of flare peak rates for the maximum and minimum phases of a 51 day period	35
Fig. 5.7	The flare frequency per day corrected for the BATSE duty cycle. Dark shading indicates periods of low activity	36
Fig. 5.8a	The differential distribution of flare peak rates for flares occurring during periods of low activity	37
Fig. 5.8b	The differential distribution of flare peak rates for flares occurring during periods of low activity	37
Fig. 5.9a	Slope of the differential distribution of flare peak rates as a function of time. Each time interval is 27 days. The data are fit with a straight line	38
Fig. 5.9b	Slope of the differential distribution of flare peak rates as a function of time. Each time interval is 25.5 days. The data are fit with a straight line	38
Fig. 5.10a	Slope of the differential distribution of flare peak rates as a function of the flaring rate. Each time interval is 27 days in size. The data are fit with a straight line	39
Fig. 5.10b	Slope of the differential distribution of flare peak rates as a function of the flaring rate. Each time interval is 25.5 days in size. The data are fit with a straight line	39
Fig. 5.11a	Flare frequency per day corrected for duty cycle for flares with $200 \text{ s}^{-1} < C_p < 351 \text{ s}^{-1}$	41
Fig. 5.11b	$351 \text{ s}^{-1} \leq C_p < 1035 \text{ s}^{-1}$	41
Fig. 5.11c	$1035 \text{ s}^{-1} \leq C_p$	41
Fig. 5.12a	Autocorrelation of daily flare rates for $200 \text{ s}^{-1} < C_p < 351 \text{ s}^{-1}$...	42
Fig. 5.12b	$351 \text{ s}^{-1} \leq C_p < 1035 \text{ s}^{-1}$	42
Fig. 5.12c	$1035 \text{ s}^{-1} \leq C_p$	42
Fig. 5.13	Haar wavelets with unit amplitude for levels $-1, 0, 1, 2, 3,$ and 4 ; for these levels there are $1/2, 1, 2, 4, 8,$ and 16 wavelets per unit interval x . The elementary wavelet is highlighted	44
Fig. 5.14	The mean square map for all BATSE flares with peak rate $\geq 200 \text{ s}^{-1}$	45
Fig. 5.15a	The time integrated mean square map for small flares	46

Fig. 5.15b	Time integrated mean square map for intermediate flares	46
Fig. 5.15c	Time integrated mean square map for large flares	46
Fig. 5.16a	The square of the wavelet amplitude at level 5 for small flares .	46
Fig. 5.16b	The square of the wavelet amplitude at level 5 for intermediate sized flares	46
Fig. 5.16c	The square of the wavelet amplitude at level 5 for large flares. The corresponding flare frequency data is included in each figure for reference	46
Fig. 5.17	The distribution of times between successive BATSE flares with peak rates $> 200 \text{ s}^{-1}$	48
Fig. 5.18	The distribution of times between successive simulated flares from the BATSE timeline with the assumption that the Sun is visible during SAA passage and earth occultation	50
Fig. 5.19	The distribution of times between successive simulated flares from the BATSE timeline with flares occurring during SAA passage and earth occultation excluded	50
Fig. 5.20	Comparison of the distribution of times between simulated randomly distributed flares and successive BATSE flares. This is the result of subtracting Fig. 5.18 from Fig. 5.16	51
Fig. 5.21	Monte Carlo simulations of sympathetic flaring. The probability that the simulated sympathetic flare distributions and the BATSE data are not drawn from the same distribution is plotted. We consider the distributions to be different when the probability is greater than 90%	52
Fig. 5.22a	The percentage of flares with peak rates $\geq 351 \text{ s}^{-1}$ as a function of time after the occurrence of the flare until the next flare. We expect 2/3 of the flares in each bin to be $\geq 351 \text{ s}^{-1}$ and the fit to the data confirms that	54
Fig. 5.22b	The percentage of flares with peak rates $\geq 1035 \text{ s}^{-1}$ as a function of time after the occurrence of the flare until the next flare. We expect 1/3 of the flares in each bin to be $\geq 1035 \text{ s}^{-1}$ and the fit to the data confirms that	54

ABSTRACT

ON THE CHARACTERISTICS OF SOLAR FLARES OBSERVED WITH THE BURST AND TRANSIENT SOURCE EXPERIMENT

by

Douglas Alan Biesecker

University of New Hampshire, December, 1994

This dissertation is an investigation of solar flare and *microflare* occurrence rates, times, and sizes in the context of solar flare occurrence models and periods, and coronal heating. Solar flares, explosive releases of energy with effects observed at earth, are not fully understood. Microflares, smaller versions of typical solar flares, were previously only observed during a short balloon experiment. They may provide clues to understanding solar flares by allowing us to test what we already know about large solar flares.

The Compton Gamma-Ray Observatory's (GRO) Burst and Transient Source Experiment (BATSE) is used to search for solar flares. This study differs from others because it is the most sensitive with a long observing time. We have used an automated algorithm to search thirteen months of BATSE discriminator data. This algorithm enabled us to detect flares at the instrumental threshold.

In this work we extend the flare size frequency distribution down to sizes smaller than previously observed in long-term experiments and find that the observed flares

are not a significant heat source for the corona. We find that the power-law shape previously measured applies to flares as small as the instrumental threshold. We test the data for systematic variations in power-law index of the flare size frequency distribution. There is only evidence for variation of the power-law index with the phase of a 51-day period.

Time series analyses are used to uncover periodic features in the daily flare occurrence rate. There is evidence for a flare size threshold effect in periodic activity. There are also characteristic activity time scales evident in the daily flare rate.

We test for randomness of solar flare occurrence and find no apparent correlation between times of flare occurrence. We also find no correlation between flare size and the time interval between flares. These findings support the avalanche flare model of Lu and Hamilton (1991) but are inconsistent with the occurrence model of Rosner and Vaiana (1978).

CHAPTER I

INTRODUCTION

Importance of Studying the Sun

The Sun, a G2 dwarf star, is quite average in its properties. The Sun holds a special place in astrophysics for only one reason; it is close enough to observe in detail with many instruments. Solar observations have been made from beneath the surface of the earth to interplanetary space. Photons and particles have been counted and images of the Sun have been constructed at all wavelengths. The Sun has even been imaged in neutrons.

Even though other high energy sources are too far away to make detailed measurements, a great deal of data has been collected from astrophysical sources of all kinds. There are two ways to interpret the data from these sources to determine what is happening. One is to model the physics from a theoretical point of view. The other is by direct observation of similar phenomena, either in a laboratory or as it occurs naturally. In a laboratory solar temperature and magnetic field magnitudes can be recreated, but the spatial scale of solar or astrophysical phenomena can never be achieved. This is where the Sun acts as a window on the universe; a natural laboratory providing a view of what processes may be taking place at remote places in the universe.

Solar Flares and Microflares

Solar flares are intense bursts of energy in the solar atmosphere that emit particles and radiation and are observable in wavelengths from radio to γ -ray. Most flares have

been observed as chromospheric brightenings in $H\alpha$. The radiation from different wavelengths may last for just a few seconds or may continue for several hours. Solar flares occur in regions of strong magnetic fields that are intimately connected with the whole flare process. The accepted idea is that a flare occurs when energy stored in the magnetic fields is released (Gold and Hoyle, 1960). Many questions surrounding flares remain unanswered; from what triggers the flare, to how the energy is released.

The general picture for solar flare X-ray production is that magnetic energy ($B^2/8\pi$) is released and goes at least partly into accelerating electrons. These fast electrons then produce high energy (hard) X-rays via non-thermal bremsstrahlung radiation. The hard X-ray photon spectrum emitted in this scenario is a power-law in energy $I(\epsilon) = a\epsilon^{-\gamma}$ when the source electron beam energy distribution also has a power-law distribution in energy $F(E) = AE^{-(\gamma-1)}$ (Brown, 1971).

Low energy (soft) X-rays are the result of thermal bremsstrahlung radiation. In a thermal source, the energy of the plasma is determined by the characteristic plasma temperature. The electrons in a heated plasma emit bremsstrahlung radiation through collisions with protons. The soft X-ray photon spectrum emitted typically has the form of an exponential in energy $I(\epsilon) = \epsilon^{-1}e^{-\epsilon/kT}$.

The initial work on small X-ray flares showed that the intensity curves of weak flares consist of many short, similar spikes (van Beek *et al.*, 1974). The concept *Elementary Flare Bursts* was introduced, where nonthermal solar flares are a superposition of many smaller *elementary* bursts. If small flares, called microflares, are the elementary component of solar flares, then studying microflares is important since they are a fundamental element of the process.

The word “microflares” was coined by Lin *et al.* (1984). During a balloon flight in 1980 they observed approximately 25 hard X-ray bursts in 141 minutes of solar observations. These flares had durations as small as a few seconds. The temporal structure of the larger bursts was consistent with them being a superposition of

smaller elementary bursts.

The advantages of investigating microflares as opposed to larger flares are that smaller flares may have simpler boundary conditions, are probably more compact and less likely to have varying properties across the flaring region, and are more likely to release their energy via one mechanism (Simnett and Dennis, 1985). Interpreting measurements of small flares should be simpler.

It has been suggested that dissipation of magnetic energy could heat the solar corona (Gold, 1964; Parker, 1972; Tucker, 1973; Levine, 1974). The solar corona at 10^6 K degrees is much hotter than the 6000 K photosphere. Energy is transported efficiently from the solar surface into the atmosphere, where it is deposited. It is not known how this takes place. Microflares could provide the energy necessary to heat the corona (Parker, 1981a, 1981b; Lin *et al.*, 1984; Parker, 1988; Hudson, 1991).

Using BATSE to Observe Solar Flares

The Burst and Transient Source Experiment (BATSE) on board the Compton Gamma Ray Observatory (GRO) can be used to observe small solar flares in X-rays. BATSE was designed to study cosmic γ -ray bursts. The instrument has a full-sky view and a large area. The design of BATSE as a sensitive detector of γ -ray bursts also makes it a sensitive detector for solar flares.

The BATSE data have two features that are advantageous for microflare observations; a long timebase (more than 3 years at the time of this writing) and directional information necessary to identify the origin of events. The independent identification of events means that BATSE data can be used without relying on data from other spacecraft or from the ground.

This study seeks to determine the characteristics of solar flare and microflare occurrence rates, occurrence times, and sizes. Listed below are the investigations reported in this thesis.

- The size distribution of flares is used to determine the role of small flares in

coronal heating. A comprehensive BATSE flare list has been constructed. In addition, selections are made to optimize observing conditions in order to extend the distribution down to the smallest flare sizes possible.

- The variability in the shape of the flare size distribution has been measured. We measure the size distribution of flares as a function of time, solar activity levels, and phase of a 51-day period.

- The data have been examined for periods in the flare occurrence rate as a function of flare size. Do small flares and large flares always occur at the same relative rates?

- Wavelet analysis is performed on the flare occurrence rate to determine the time scales on which solar activity occurs.

- This study tests predictions of the avalanche model of solar flares (Lu and Hamilton, 1991; Lu *et al.*, 1993) that states that the time between successive flares is independent of the size of either flare. Another prediction of the model is that the flare size distribution has a constant power-law slope. We also test predictions of the stochastic model of Rosner and Vaiana (1978).

CHAPTER II

THE SUN

To completely understand solar flares one must understand the environment in which they occur. Magnetic fields, which play such an important role in solar flares, are present in both the solar interior and atmosphere. How these regions are connected and influence flare activity must be understood. The development of solar flares and magnetic fields in the solar atmosphere may depend on where and how the magnetic fields are developed beneath the surface.

The Interior

The interior of the Sun is hidden from our view, however, researchers have been able to deduce much about the interior from a paucity of data. The Sun's size, mass, surface temperature, and elemental composition are all determined relatively easily.

Recently, neutrinos and solar oscillations have been used to probe the solar interior. These measurements are sufficient to confirm that the interior of the Sun is composed of three distinct regions: the core, the radiation zone, and the convection zone (Fig. 2.1). Most important for solar flares, the magnetic fields are generated in the solar interior.

The primary energy source of the Sun is fusion of H into He ($4^1H \rightarrow ^4He$) within the core. The mass lost in the conversion from four H nuclei to one He nucleus releases 4×10^{-5} ergs or 25 MeV of energy. At the Sun's present luminosity, the hydrogen is expected to last for 10 billion years. The core of the Sun has a radius of $\lesssim 0.3$ solar radii (R_{\odot}) containing $\sim 60\%$ of the mass of the Sun.

The radiation zone lies above the core and has a thickness of about $0.45R_{\odot}$. The properties of the region are such that radiation is the main energy transport mechanism. The temperature, density, and pressure all decrease with radius. The mean free path of photons in the radiation zone is only a few centimeters, so the photons created in the core are scattered on the order of 10^{21} times on their journey through the radiation zone. On average, photons lose energy in the scattering process, starting out as γ -rays and leaving the Sun at visible light energies.

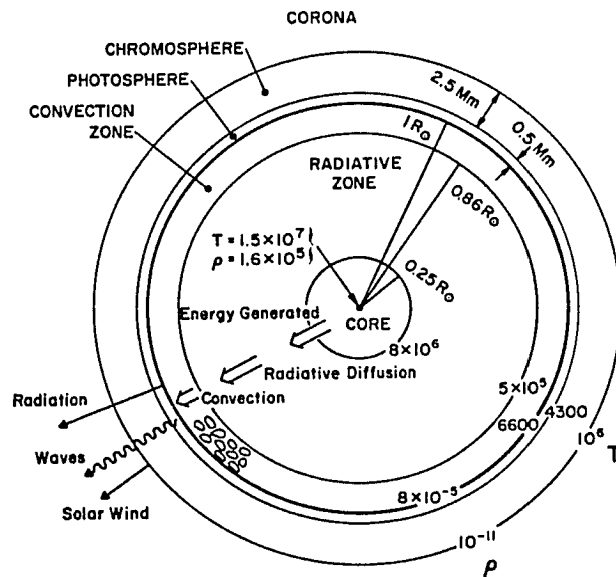


Fig. 2.1. The overall structure of the Sun, indicating the sizes of the various regions and their temperatures (in degrees K) and densities (in kg m⁻³). The thicknesses of the photosphere and chromosphere are not to scale (Priest, 1982).

Above about $0.75R_{\odot}$, convection becomes the dominant energy transport mechanism. The opacity of the region increases because atoms are not fully ionized. The temperature gradient becomes steep and the rising parcels of gas, which cool due to expansion as they rise, remain hotter than the surrounding gas and continue to rise. At the top of the convection zone the gas gives up some of the energy acquired at the bottom of the convection zone and then sinks back down. Energy is thus convected

through this region to the solar surface.

It is within or just below the convection zone that the magnetic field of the Sun is believed to be generated. In what is known as a dynamo, magnetic fields are maintained by currents induced by plasma motion. The motions in the convection zone act to intensify the magnetic field by stretching and twisting it.

The Atmosphere

The solar atmosphere consists of the photosphere, the chromosphere, the transition region, and the corona. The properties of each of these regions are different, but the boundaries between the regions are neither clearly resolved nor static. The regions are commonly identified in terms of densities and temperatures.

The top of the convection zone occurs where the opacity of the gas drops to an optical depth of one at a wavelength of 5000\AA . $\tau_{5000} = 1$ is the surface of the Sun that is seen with the naked eye. This is the lower edge of the photosphere, where the temperature is about 6500 K. Above this altitude the temperature falls, but then increases after a minimum of about 4400 K at an altitude of ≈ 500 km above $\tau_{5000} = 1$. The temperature profile for the solar atmosphere is illustrated in Figure 2.2. The average density drops monotonically through all layers of the atmosphere.

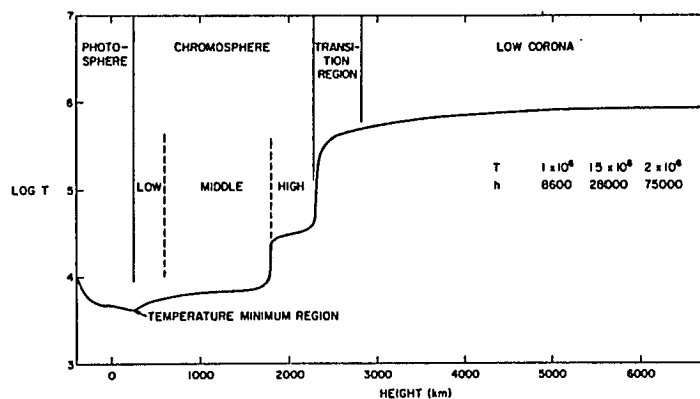


Fig. 2.2. An illustrative model for the variation of the temperature with height in the solar atmosphere (Athay, 1976).

The chromosphere is bounded on the bottom by the temperature minimum and

on the top by the transition region. The thickness of the chromosphere is only on the order of 1000 km. The temperature increases slowly with height.

About 2000 km above the bottom of the photosphere lies the transition region. The transition region is identified by an extremely rapid rise in temperature from chromospheric values to coronal values of a few million degrees. There is a proportional drop in density in the transition region. The thickness of the transition region is hard to measure directly and is inferred to be a few 100 kilometers because of the large temperature and density differences between the chromosphere and the corona.

The solar corona begins at the top of the transition region and continues out into interplanetary space, where its extension is the solar wind. From a few million degrees the temperature drops off slowly out into interplanetary space because of dynamic expansion. It is not clear how the heating takes place to keep the corona so hot. The high temperature of the corona results in a very high thermal and electrical conductivity, keeping the corona at a fairly uniform temperature. The gas even in the low corona is tenuous, with a number density of $\sim 10^{10} \text{ cm}^{-3}$ (the gas density at the earth's surface is $\sim 10^{19} \text{ cm}^{-3}$). The corona has three major kinds of structures which are distributed across the surface: active regions, at low to middle latitudes, which are characterized by strong, closed magnetic fields; quiet regions, at low to middle latitudes, which are characterized by weak, closed magnetic fields; and coronal holes, typically at the poles, which are characterized by weak, open magnetic fields (Withbroe and Noyes, 1977). Active regions are where almost all flares occur. Coronal holes are observed to be a source of high speed solar wind (Krieger *et al.*, 1973; Neupert and Pizzo, 1974; Nolte *et al.*, 1976).

Magnetic Fields

Average field strengths on the Sun are $\sim 2 \text{ G}$. In sunspots however, magnetic fields of $\sim 2500\text{--}5000 \text{ G}$ are measured. In active regions the gas pressure is much less than the magnetic pressure. The ratio of the plasma gas thermal pressure to the

magnetic pressure is known as the plasma β . Below the photosphere the gas pressure dominates, $\beta > 1$, and the frozen-in-flux condition forces the magnetic fields to move with the plasma. When $\beta < 1$, as in the corona, the magnetic pressure dominates and the magnetic field lines can diverge to fill the whole corona, as shown in Figure 2.3. In the photosphere, magnetic field lines are organized into flux tubes in which the magnetic field strength is very high. The regions outside of flux tubes are usually considered to be field-free. The magnetic pressure begins to dominate the gas pressure in the chromosphere. At ≈ 1500 km above $\tau_{5000} = 1$ the flux tubes fan out, losing their individual identity, forming a canopy of magnetic field at the top of the chromosphere.

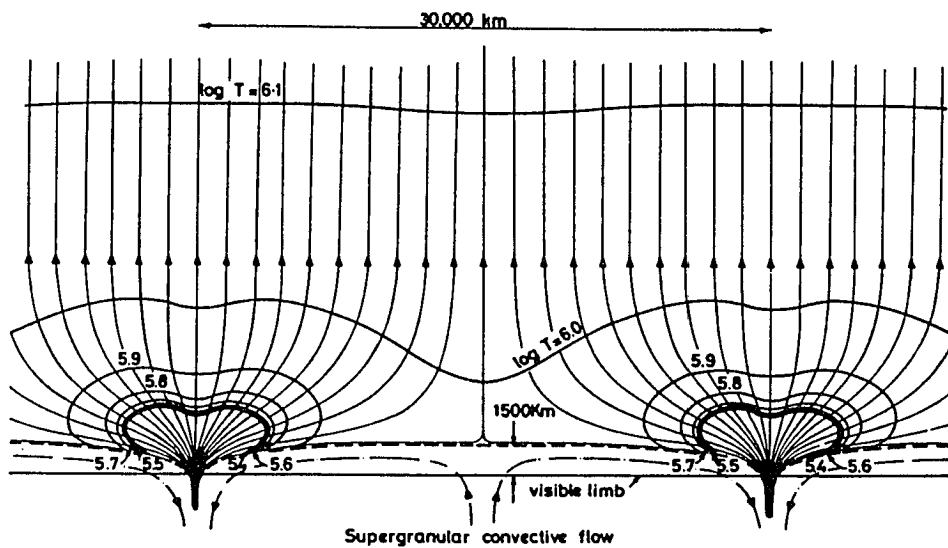


Fig. 2.3. The structure of a magnetohydrostatic network model. Temperature contours between $\log T = 6.1$ and $\log T = 5.4$ are marked (Gabriel, 1976).

The behavior of the fields at all heights of the atmosphere and beneath the photosphere play a role in solar flares. Magnetic fields in the solar atmosphere certainly play a dominant role in flares. The magnetic topology influences the triggering and development of flares. The motions in the photosphere in particular act to stress and shear the fields, changing the shape of magnetic flux tubes thereby storing energy.

CHAPTER III

SOLAR FLARES

General Flare Picture

Photospheric motions and magnetic fields are implicated as the energy source for solar flares because only they can produce the 10^{32} ergs needed for a very large flare (Gold and Hoyle, 1960). Other potential sources of energy, such as the thermal energy in the pre-flare plasma and gravitational potential energy do not provide enough energy. Nuclear burning cannot occur because pre-flare temperatures and densities are not great enough. In addition, a more direct argument can be made implicating magnetic fields in the flare process. That is, flares occur in active regions (AR), areas of high magnetic field. Furthermore, ARs with complex field structures are more likely to produce large flares. There is an 11 year period in the number of ARs and solar flares.

Even though magnetic fields are the probable means of energy storage, it is not known how, or where, the energy is released. What is known, is that the energy release can be rapid and energetic. Electrons and protons are simultaneously, or nearly so, accelerated to MeV energies (Forrest and Chupp, 1983). Photons are emitted from radio to γ -ray wavelengths and solar plasma is heated to $> 10^7$ K. Some possible mechanisms for accelerating the particles are DC E-field acceleration, stochastic acceleration by plasma waves, or shock wave acceleration. The two most popular models for the origin of X-ray photons are thermal and non-thermal bremsstrahlung.

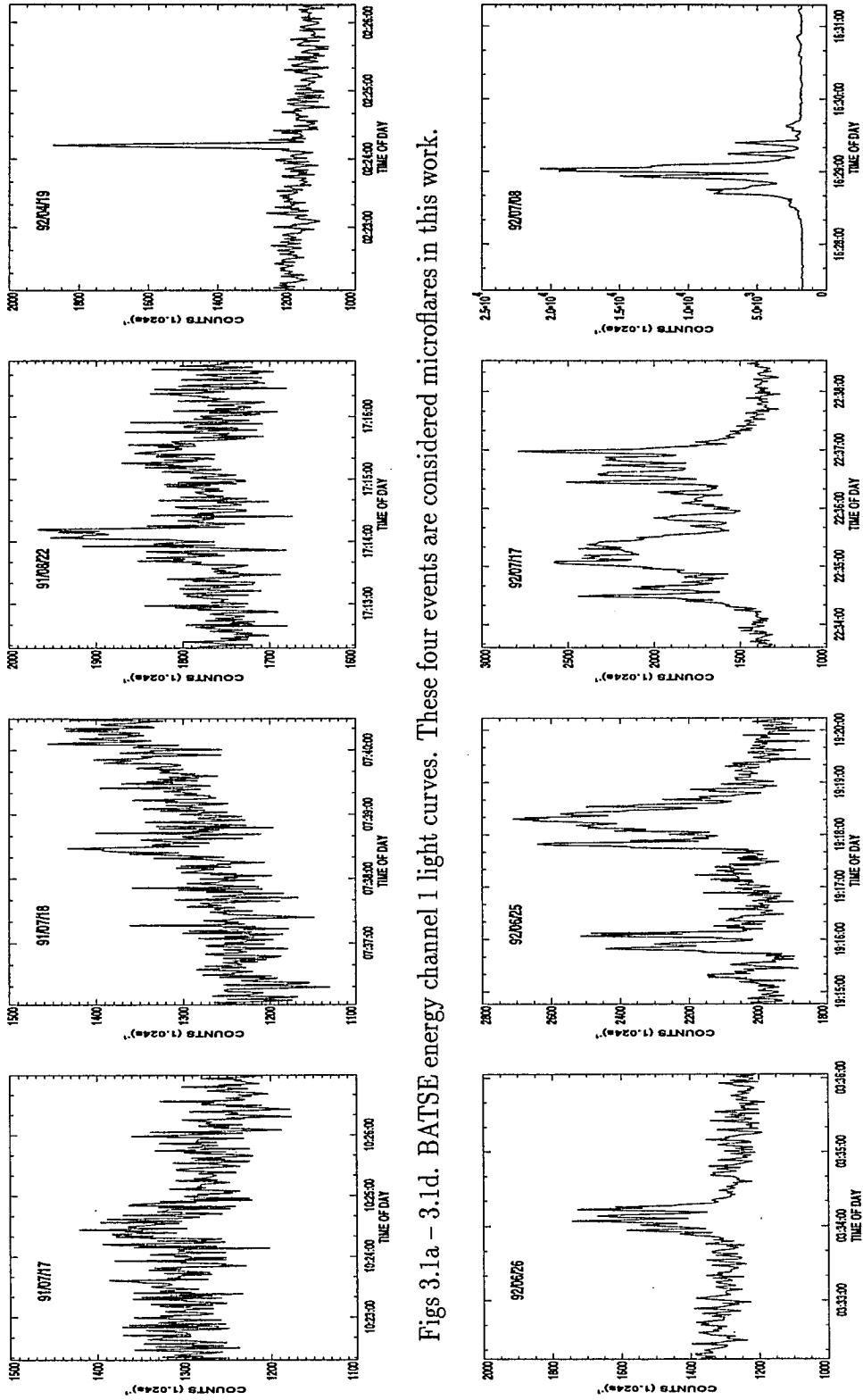
Microflares

The basic definition of microflares and motivation for studies of them were outlined in Chapter I. In Figures 3.1a–h, the ‘Elementary Flare Burst’ (EFB) concept is illustrated using BATSE Large Area Detector ($\sim 25\text{--}50$ keV) data. The first four Figures (3.1a–d) show microflare events with various full width at half maximum (FWHM) durations. Comparing these four microflares to the structure in the four flares in Figures 3.1e–h, it is clear that the more complicated events could easily be constructed by a superposition of such events (van Beek *et al.*, 1974).

De Jager and de Jonge (1978) found that weak flares could be decomposed into short-lived bursts, whereas strong flares were difficult to decompose. They studied 8 weak flares and found that the individual EFBs within each flare had approximately equal FWHMs; however, the average EFB FWHM varied from flare to flare (4–24 seconds). They also found that there was no correlation between the FWHM of EFBs and their intensity. There was also no systematic variation of the FWHM of EFBs with time in a flare.

Further measurements of small flares were conducted in 1980 and 1987 with a sensitive balloon-borne, X-ray instrument developed at UC Berkeley (Lin *et al.*, 1984, 1991). The first flight during solar maximum detected ~ 25 hard X-ray events with fluxes $> 7 \times 10^{-3} \text{ cm}^{-2} \text{ s}^{-1} \text{ keV}^{-1}$ at 20 keV (141 minutes of data). They coined the term *microflares* to describe the small events observed. The energy spectra of the larger bursts were fit with power-law shapes, $AE^{-\gamma}$, with $\alpha \sim 4$ to 6. The total energy in these events, assuming a non-thermal, thick target model, was on the order of $10^{26}\text{--}10^{28}$ ergs. The small structures that comprise the larger events had shorter FWHM (1–2 sec) than those measured by de Jager and de Jonge (1978).

Plotted in Figure 3.2 is the integral size distribution of event peak rates for the Lin *et al.* events. The slope of the distribution is reported to be ~ -1 . The distribution of flare sizes measured earlier with OSO-7 is also shown on the plot.



Figs 3.1a – 3.1d. BATSE energy channel 1 light curves. These four events are considered microflares in this work.

Figs 3.1e – 3.1h. BATSE energy channel 1 light curves. These four events are examples of flares that could be constructed from a superposition of microflares.

The OSO-7 distribution, from Datlowe *et al.* (1974), is for 123 hard X-ray bursts detected from October 1971 to June 1972. The difference in amplitude in the two observations is due to variations in the overall flare rate. The second flight of the UC Berkeley instrument, which occurred during solar minimum, did not detect any microflares in 16.5 hours of observations, providing further evidence for variability with the solar cycle.

These observations in X-rays define microflares. However, one of the keys to fully understanding microflares lies in observing associated emission at other wavelengths.

During the first Lin *et al.* balloon flight, concurrent observations were made in $H\alpha$ at Sacramento Peak Observatory (Canfield and Metcalf, 1987). With a small field-of-view, their observing strategy was to point at a region that was flaring and then re-point to another region as it flared. Thus, any overlap with the Lin *et al.* experiment was by chance. They saw ~ 6 $H\alpha$ events associated with the 25 hard X-ray events. The morphology and duration of the $H\alpha$ events were reported to be like usual $H\alpha$ flares, only smaller. Records of radio observations during the balloon flight show that only four of the microflares had accompanying radio emission. Three events showed type III bursts and one of those plus a fourth event had accompanying emission at 7 GHz (Lin *et al.*, 1984). Type III bursts, which are common, are observed in radio wavelengths from tens of kHz to hundreds of MHz and are seen as a fast drift (20 MHz s^{-1} @100 MHz) from high to low frequency. They are produced by streams of ($> 10 \text{ keV}$) electrons moving upward through the corona, exciting plasma oscillations at the plasma frequency.

Simnett and Dennis (1985) reported on observations of fast, soft X-ray spikes observed by the Solar Maximum Mission's Hard X-ray Imaging Spectrometer (3.5–8.0 keV) and the Hard X-ray Burst Spectrometer ($> 28 \text{ keV}$). They found no consistent correlation of soft X-rays (3.5–8.0 keV) with hard X-rays ($> 28 \text{ keV}$), microwaves, $H\alpha$, or type III emissions. Some of the soft X-ray events had no observable emission

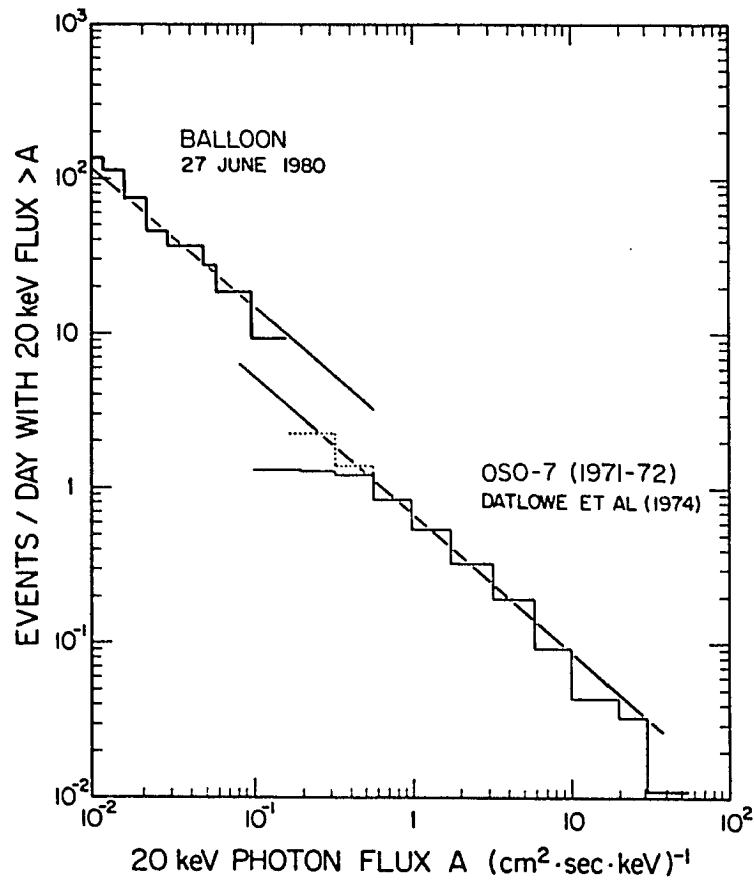


Fig. 3.2. The distribution of the integral rate of occurrence of events vs. peak 20 keV photon flux for the solar hard X-ray microflares observed in this balloon flight. Also shown for comparison is the distribution of solar flare hard X-ray bursts reported by Datlowe, Elcan, and Hudson (1974) (Lin *et al.*, 1984).

at any other wavelength. Since many of the events had no accompanying hard X-ray emission, there is no clear connection between these events and the Lin *et al.* microflares. The Lin *et al.* balloon experiment was more sensitive than HXRBS because of a larger detector area and better background rejection by use of a Phoswich detector. In addition, HXRBS had aluminum in front of the detector, as well as a CsI dead layer in the front of the main detector crystal, reducing the detection efficiency of photons < 30 keV (Orwig *et al.*, 1980). It may be that the Simnett and Dennis soft X-ray events were too weak to be detected by HXRBS or that not all flares accelerate electrons.

Ultraviolet observations of solar active regions have revealed frequent, small, short transient brightenings (Porter *et al.*, 1984, 1987). These brightenings have FWHM durations as small as 20 s and have spatial sizes less than $3'' \times 3''$. These events are not associated with any hard X-ray emission, though they may just be too weak for hard X-ray instruments to detect. Earlier observations have shown a correlation between UV and hard X-ray flares (Cheng *et al.*, 1984; Poland *et al.*, 1984).

Radio observations of the Sun made with the Very Large Array measured many small microbursts at 1.4 GHz (Bastian, 1991). Some tens of microbursts were seen in 65 minutes of observations. These events had durations from < 10 to 40 seconds and spatial sizes from $15''$ to $34''$. They all occurred within sunspots. Again, there is no clear connection between these small radio events and X-ray microflares, possibly because of the small size of the events.

CHAPTER IV

THE EXPERIMENT

Instrumentation

Compton Gamma Ray Observatory

The Compton Gamma Ray Observatory was placed in orbit in April 1991. The spacecraft has been operating continuously since then, with some loss of data in 1992 due to failure of the on-board tape recorders. The spacecraft is in a low earth orbit (350–450 km) with an inclination of 28°. On board are four instruments that observe in hard X-rays to γ -rays (Kniffen, 1989). Two of the instruments are telescopes and are fixed to point parallel to the spacecraft z-axis. In order for these instruments to observe different sources, the entire spacecraft must be rotated. The spacecraft normally points in one direction for one or two weeks at a time.

Burst and Transient Source Experiment

The BATSE Large Area Detector (LAD) data are used in this work (Fishman *et al.*, 1989). The Burst and Transient Source Experiment consists of eight modules placed on the corners of the spacecraft (Figure 4.1). As seen in Figure 4.2a, each module contains a Large Area Detector and a Spectroscopy Detector (SD). The LADs are arranged so that the faces of the detectors are parallel to the faces of a regular octahedron (Figure 4.2b). Every point in space is thus viewed by four detectors.

The LADs are NaI(Tl) scintillators and are uncollimated, passively shielded in the rear (Figure 4.2a). The front of each LAD is covered with a plastic scintillator to reject charged particle events. Each NaI(Tl) scintillator has a frontal area of 2025 cm²

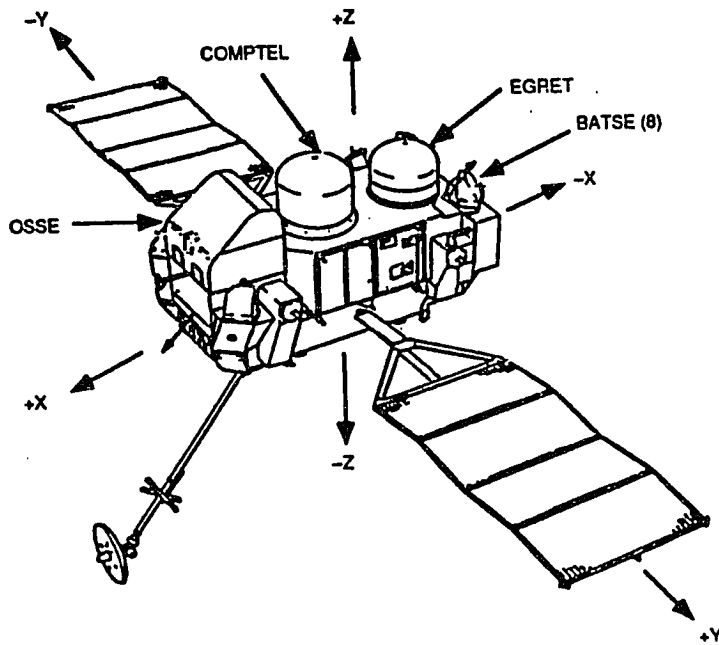


Fig. 4.1. A sketch of the COMPTON Gamma Ray Observatory showing the four instruments. The 8 BATSE modules are located on the corners of the spacecraft. The spacecraft coordinate system is also shown (Fishman, 1992).

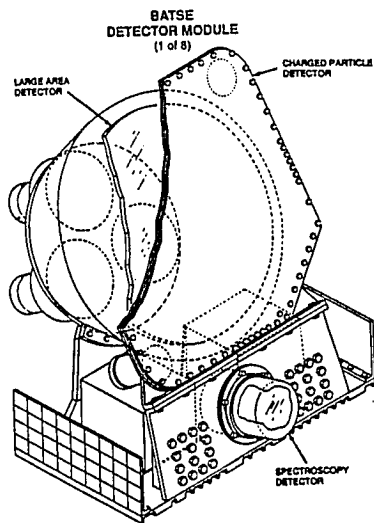


Fig. 4.2a. Drawing of a BATSE detector module consisting of a Large Area Detector and a Spectroscopy Detector (Fishman, 1989).

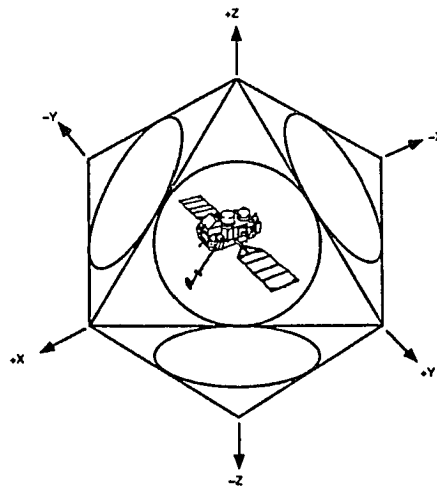


Fig. 4.2b. The BATSE detector aspect is illustrated (Fishman, 1989).

and a thickness of 1.27 cm. The LAD data are divided into four energy channels: 25–50, 50–100, 100–300, and 300–1900 keV. Count rate data are recorded continuously with a time resolution of 1.024 seconds. The Spectroscopy Detectors are not used in this research.

The orbit of GRO results in a duty cycle for solar viewing of ~ 0.55 . This is because the earth blocks the solar viewing direction during $\sim \frac{1}{3}$ of each orbit and because the spacecraft passes daily through the South Atlantic Anomaly during some orbits. Figure 4.3 shows the BATSE solar viewing duty cycle for the period covered in this work. The date system used is a truncated julian date (TJD) defined as (julian date)–2440000.5 (TJD=0 on 24 May 1968 at 0UT). Periodic variations in the viewing fraction are due to the ~ 45 day precession of the spacecraft orbit. On 17 Mar 92, there was a failure of the on-board tape recorders, reducing the duty cycle to ~ 0.35 (see Fig. 4.3).

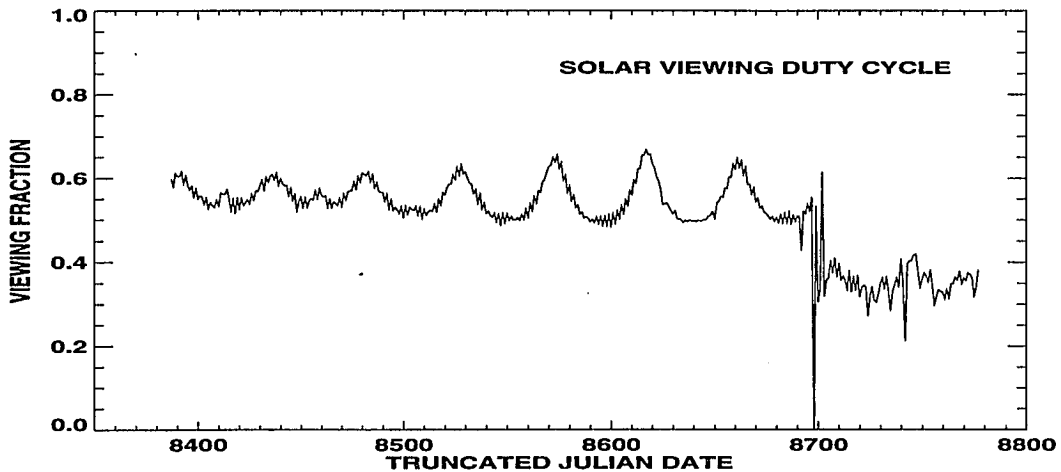


Fig. 4.3. The solar viewing duty cycle is plotted for the truncated julian dates 8387 through 8777.

Data Processing

Flare Search

Flares and microflares are present in the data as transient count rate increases (Fig. 3.1). The BATSE LAD data are examined for solar flares on a daily basis at the

Solar Data Analysis Center (SDAC) at NASA/Goddard Space Flight Center. This search is performed by checking visually the light curves of the solar facing detectors for count rate increases. In order for the search to be accomplished in a reasonable amount of time the data are plotted for one spacecraft orbit at a time and visible count rate increases (peaks) are investigated at a finer time scale (Fig. 4.4). Generally, a flare must appear in only the solar facing detectors (the peak rate decreasing with detector incidence angle) and must have also been measured by the Geostationary Operational Environmental Satellites (GOES) X-Ray Monitors. The GOES spacecraft monitor the whole Sun flux in two energy bands 0.5–4Å and 1–8Å. Flares found in this way are compiled on a list made available by the SDAC, hereafter referred to as the SDAC list.

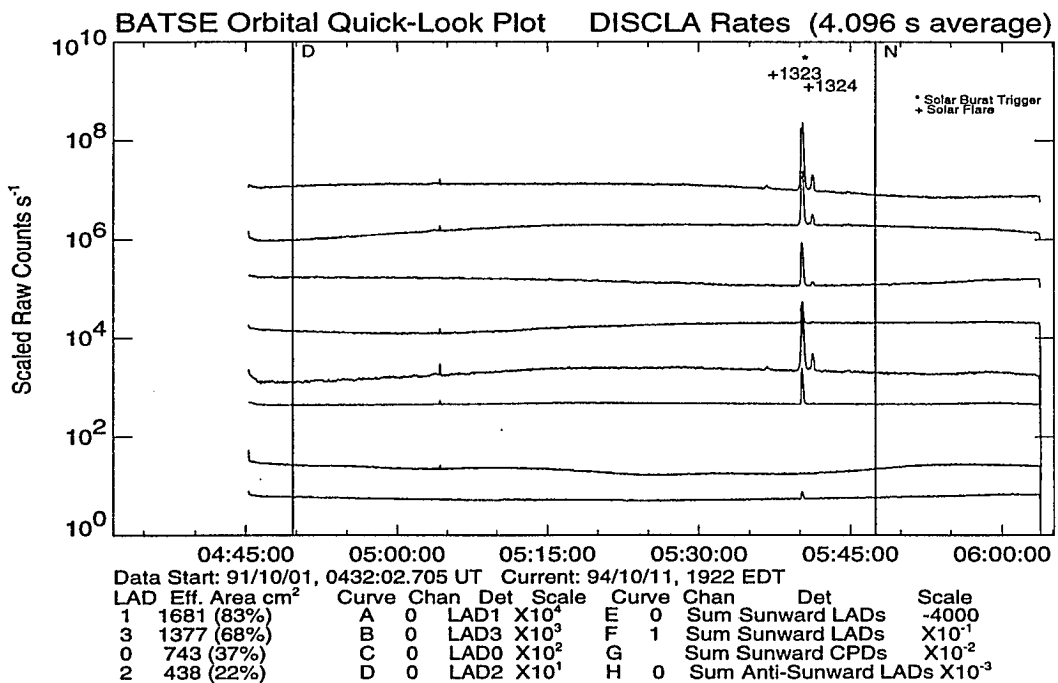


Fig. 4.4. A sample BATSE light curve available from the Solar Data Analysis Center. The data from one spacecraft orbit are shown. The 8 scaled light curves are, from top to bottom, the first energy channel of the four solar facing detectors, the summed solar facing detectors first two energy channels, the summed solar facing charged particle detectors, and the summed non-solar facing detectors first energy channel.

This thesis is able to improve on the work of the SDAC search by use of an automated search algorithm that takes advantage of the BATSE source location ability. The automated algorithm allows us to analyze many peaks quickly, so we are able to search for flares that are much smaller than those found by the visual search. The number of peaks increases rapidly with decreasing event size, due to an increase in the number of actual solar flares and to an increase in the number of non-solar events. The automated search also has the advantage of avoiding subjectivity.

The algorithm consists of two parts. The first is the detection of count rate increases by calculating the second derivative in time of the count rate (Mariscotti, 1967). The second is to determine if the count rates in the solar facing detectors are consistent with a source in the solar direction.

The method to identify rate increases is based on taking a simple second time derivative which locates the maxima and minima of a function. This method is used because it is independent of background. Since the BATSE data are discrete the second difference is used.

Over short enough intervals the background count rate is changing linearly with time. The second derivative in this case is independent of background. If $N(t)$ represents the total count rate, $G(t)$ is the rate due to a solar flare, and $B + Ct$ describes a linearly changing background rate

$$\text{then } N(t) = G(t) + B + Ct, \quad (4.1)$$

$$\text{and } \frac{\partial^2 N}{\partial t^2} = \frac{\partial^2 G}{\partial t^2}, \text{ where} \quad (4.2)$$

the second difference S_i is given by

$$\frac{\partial^2 N}{\partial t^2} \equiv S_i = N_{i+1} - 2N_i + N_{i-1}, \text{ and} \quad (4.3)$$

N_i is the detector counts in time interval i . The time interval for each data point i is the same, so the detector rates are assumed to be counts. The standard deviation of

the second difference is given by

$$F_i = \sqrt{N_{i+1} + 4N_i + N_{i-1}}. \quad (4.4)$$

To improve the sensitivity of the search, the signal to noise ratio S_i/F_i can be enhanced through some simple smoothing techniques. The first is to smooth the data by averaging over the M nearest measurements before and after time interval i .

$$\bar{S}_i = \sum_{j=i-M}^{i+M} S_j. \quad (4.5)$$

We will later vary M .

Additional gain is made by subsequently averaging the values \bar{S}_i over Z of its nearest neighbors,

$$S'_i = \underbrace{\sum_{j=i-M}^{i+M} \cdots \sum_{h=l-M}^{l+M}}_Z S_h. \quad (4.6)$$

The significance of count rate increases is measured by the value of W ,

$$W = \frac{S'_i}{F'_i}. \quad (4.7)$$

Signal to noise improvements in W are greatest when $Z = 4$, with little improvement for higher Z values (Mariscotti, 1967). Plotted in Figure 4.5 is a comparison of a raw BATSE light curve, the unsmoothed \bar{S}_i/\bar{F}_i , and the smoothed S'_i/F'_i for $M = 8$ and $Z = 4$.

The value of W is determined for each data point in the two most solar facing BATSE detectors. Any data point that has $W \geq 3$ in a single detector or $W \geq 2.5$ in both detectors is considered to be significant if it is also a local maximum. We refer to these as “triggers.”

The search for triggers in the data is conducted with a fixed value of $Z = 4$ but varying M over the values 4, 8, 16, and 32. The choice of M determines the characteristic peak width or event duration of the search, *e.g.* large M values represent long, slowly varying events.

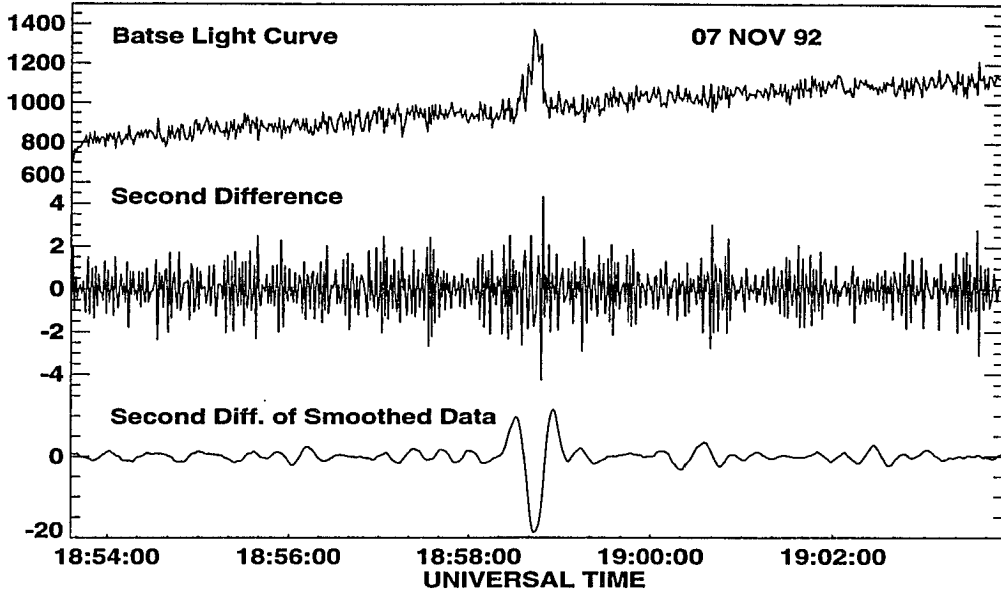


Fig. 4.5. A sample of the raw BATSE data, its second difference, and second difference of smoothed data are shown. The top light curve is the BATSE count rate for the first energy channel of the most solar-facing detector. The middle curve is the second difference of the count rate divided by the standard deviation of the second difference. The bottom curve is W (Eq. 4.7), for $M = 8$ and $Z = 4$.

In practice, the smoothed second difference and its standard deviation are calculated by a set of coefficients C_{ij} used to multiply the count rate in each time bin i (Fig. 4.6). The coefficients used to calculate the unsmoothed second difference are easily seen to be 1, -2 , and 1 (from Eq 4.3). Each element of the coefficient array C_{ij} is multiplied by the appropriate count rate data point j and then summed to calculate the second difference at point i .

$$S'_i = \sum_j C_{ij}(M, Z)N_j, \text{ and} \quad (4.8)$$

$$F'_i = \left[\sum_j C_{ij}^2(M, Z)N_j \right]^{\frac{1}{2}}, \text{ where} \quad (4.9)$$

$$C_{ij}(M, Z) = \sum_{k=i-M}^{k=i+M} C_{kj}(M, Z-1), \text{ and} \quad (4.10)$$

$$C_{ij}(M, Z = 0) = \begin{cases} 0 & \text{if } |i - j| > 2 \\ 1 & \text{if } |i - j| = 1, \text{ and} \\ -2 & \text{if } i = j \end{cases} \quad (4.11)$$

$$C_{ij} = 0 \text{ whenever } |i - j| > (M + 1)Z. \quad (4.12)$$

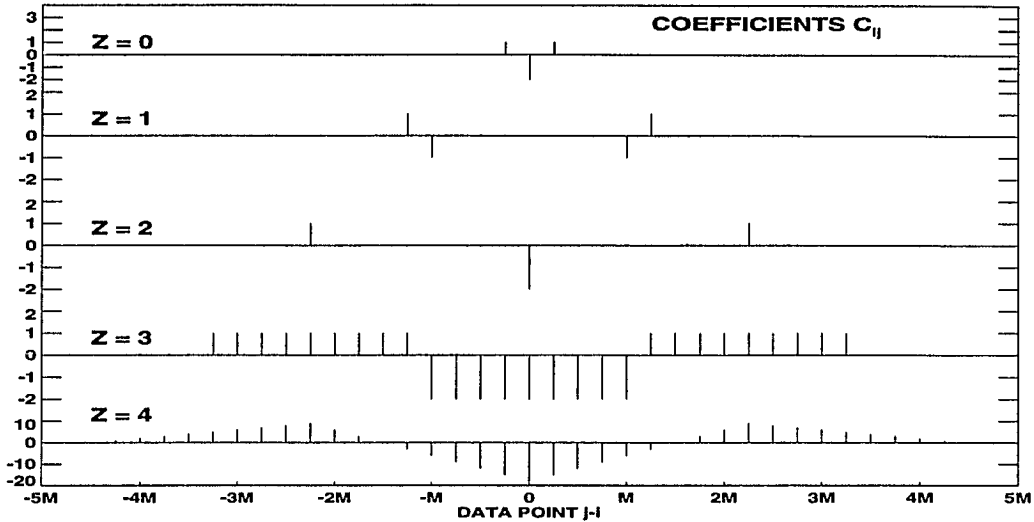


Fig. 4.6. The second difference coefficients C_{ij} are shown for the cases where $Z = 0, 1, 2, 3,$ and 4 . The $Z = 0$ case is described by Eq. 4.3. The coefficients for $Z > 0$ are higher order smoothing cases. The $Z = 4$ case is used for this work.

Source Location

After the triggers are identified, it is necessary to test the data to determine if the events are of solar origin. This is where the BATSE instrument has its biggest advantage over other non-imaging instruments. Four detectors view the Sun, each with a different projected area toward the Sun. The event rate in each detector is proportional to the detector area normal to the Sun. A measure of this proportionality (R) is used to identify solar flares (where $R = 1$ for solar flares after correcting for angular response).

$$R_{j1} \equiv \frac{\text{counts in detector } j}{\text{counts in most solar facing detector}}. \quad (4.13)$$

In testing the data, we found that the source counts in each detector are not proportional to the projected detector area to the source. There are several possible

reasons for this discrepancy; the most likely one for solar flare analysis is that the individual detectors have different hardware thresholds in the first energy channel.

The process of identifying triggers involves several steps, the end result of which is to identify each trigger with a single number (\bar{R}) that indicates whether or not the event is solar in origin. The first step is to determine a correction factor (K) for each detector that accounts for the discrepancy between the source counts and the projected area of each detector.

Detector correction. Solar flares that have been cataloged on the SDAC list are used to determine the correction factor (K_j) for each detector j . K_j is used to scale the measured count rates. The value of K_j is defined such that $R'_{j1} \equiv 1$ and is determined as follows

$$R'_{j1} = R_{j1} \times K_j = \frac{\text{counts in detector } j \times K_j}{\text{counts in most solar facing detector}} \quad (4.14)$$

We assume that the count rate differences between detectors that do occur are consistent throughout each GRO viewing period, but that they change when the spacecraft is repointed. Because of this correction factors are calculated for each orientation of the spacecraft. To determine the correction factors for each viewing period, the average R'_{j1} over many flares is set equal to one.

Not all flares are necessarily used to determine K_j . If there are differences in flares as a function of size then these differences are minimized by using only small flares to compute the correction factors. In addition, for viewing periods with many known flares, only a subset of them were used to determine the correction factors.

Possible reasons for why the correction factors K_j are necessary include differences in the individual detectors, atmospheric scattering effects, and incorrect detector angular response. The hardware thresholds of the individual detectors are different at the low energy edge of the first energy channel. This causes the detectors with lower thresholds to record greater numbers of photons from a given source than a detector with higher thresholds. For solar flares, the effect is greatly magnified because flare

photon spectra are very steep with the flux per unit energy bin increasing rapidly with decreasing energy. Effects due to atmospheric scattering should be greatest in the energy range covered by channel 1 of the LADs, however the scattering should be insignificant for small flares, especially with the steep power law photon spectrum of solar flares. There are few, if any high energy photons to be scattered down to lower energies. Another consideration is that there could be an azimuthal angular response dependence in the detectors (Pendleton *et al.*, 1989). Regardless of the reason, it is important to cross-calibrate the detectors for each spacecraft orientation.

Trigger identification. Once the correction factors have been determined for the solar-facing detectors they can then be applied to all of the triggers to search for unidentified solar flares. For each trigger the following steps are taken to identify the trigger origin.

Data centered on the trigger time are used to fit the background to a polynomial. We have chosen 10 minutes as an appropriate background sample. We must ensure that there are sufficient background counts before and after the event for an adequate fit. However, the data interval must be kept short so that there will be only one event in the interval. If there are gaps in the data, the interval is shortened to avoid the missing data. The algorithm fits the ten minute data interval iteratively. After each iteration, all data $> 3\sigma$ above the fit are removed. This is repeated 10 times or until there are no more problem data points. We require that the background rate be $> 800 \text{ s}^{-1}$ and $< 2200 \text{ s}^{-1}$, the normal range of BATSE LAD channel 1 background rates. This ensures that the automated fit routine works properly. The data from all 4 solar facing detectors are fit.

The fit procedure was tested on known flares from the SDAC list. The fit algorithm works well for flares less than a few minutes in duration, however larger events must be fit manually.

From the residual, the total counts within $\pm M$ data points of the trigger are used

to determine the event origin. The total counts in the $\pm M$ window are corrected for angular response, assuming a solar origin. The detector correction (K_j) is then applied to the total counts in each detector. A weighted average count ratio \bar{R} calculated for each trigger is used to identify flares. \bar{R} is defined as

$$\bar{R} = \frac{\sum_{j=2}^4 \frac{R'_{j1}}{\sigma_{R'_{j1}}^2}}{\sum_{j=2}^4 \sigma_{R'_{j1}}^{-2}}. \quad (4.15)$$

Plotted in Figure 4.7 is the mean ratio of counts \bar{R} for each trigger detected by the algorithm. The peak in the distribution centered on $\bar{R} = 1$ is due to solar flares.

To compile the solar flare list used in this thesis we made selections on the data requiring $0.71 < \bar{R} < 1.41$. Also, since the algorithm may trigger several times on individual flares if they are sufficiently long or have multiple peaks, we consider triggers that are separated by less than two minutes to be part of the same flare. The algorithm with these criteria correctly identifies 95% of the flares on the SDAC solar flare list.

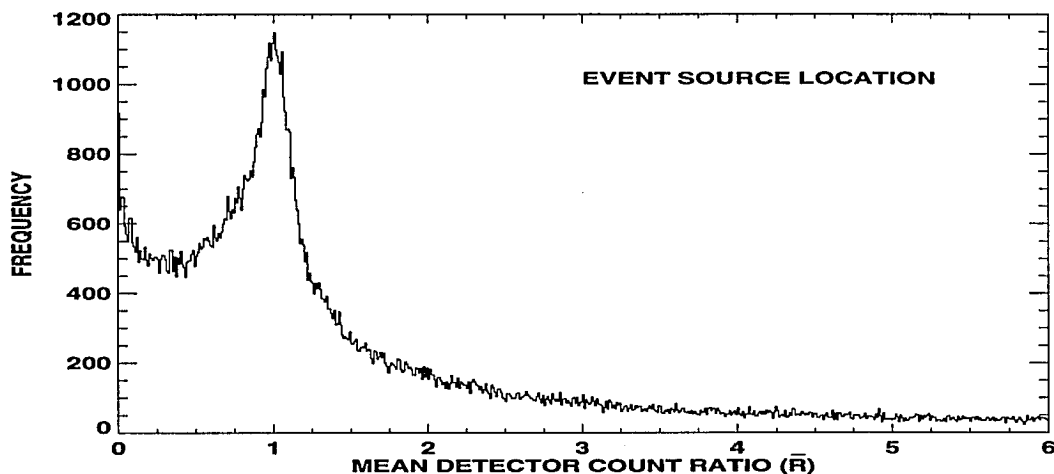


Fig. 4.7. The weighted average of the normalized count rates in the solar-facing detectors. A value of 1.0 identifies events that are consistent with the solar direction.

The flare identification method is tested by searching for flares when CGRO is in the earth's shadow. Using data from a two week period we searched for triggers

consistent with a source in the solar direction during spacecraft night. We searched a total of 6338 minutes of night-time data. The data from each trigger were processed in exactly the same manner as data obtained during spacecraft day. The distribution of detector count ratios is plotted in Figure 4.8a. The same analysis was performed on 6338 minutes of data from daylight portions of the orbit for the same two weeks (Figure 4.8b). There is an obvious peak in the distribution near $\bar{R} = 1$. We attribute the entire excess around $\bar{R} = 1$ to solar flares. The distributions are approximately equal away from the value 1.0.

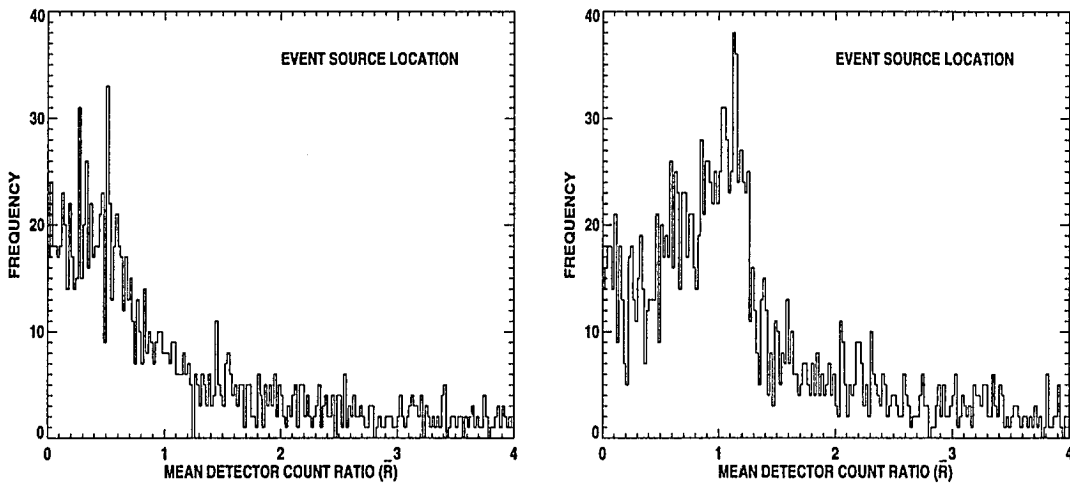


Fig. 4.8a. The weighted average of the normalized count rates in the solar-facing detectors. A value of 1.0 indicates events that are consistent with the solar direction. The triggers were detected when the spacecraft was in the earth's shadow.

Fig. 4.8b. The weighted average of the normalized count rates in the solar-facing detectors. A value of 1.0 indicates events that are consistent with the solar direction. The triggers were detected on the day side of the earth.

CHAPTER V

ANALYSIS AND RESULTS

This section is divided into three categories: flare frequency distributions, time series analyses, and avalanche theory testing.

Flare Frequency Distributions

We examine the size distribution of flares in a variety of ways. First, the size distribution of flares is found for the whole BATSE data set. Next, the sensitivity limit of the detectors is determined. The size distribution is then extended down closer to the limit of the detectors. The power-law index of the size distribution of flares is then tested for variability in several ways. Finally, size distributions are constructed as functions of the phase of a presumed 51-day period in solar flare occurrence (Bai, 1994), of flaring rate, and of time.

Differential Distribution of Flare Peak Rates

All data. The differential distribution of peak flare rates has been plotted in Figure 5.1 for all of the flares measured with BATSE between TJD 8387 (11 May 91) and 8777 (04 Jun 92). The data are well fit with a power-law in peak count rate. The power-law spectral index is found to be -1.68 ± 0.02 . This power-law result, within uncertainties, is the same as that reported by earlier researchers (Datlowe *et al.* 1974; Lin *et al.* 1984; Dennis 1985; Schwartz *et al.* 1992; Crosby *et al.* 1993). However, the result here extends the distribution down to peak rates that are about an order of magnitude smaller than earlier, long term experiments. The threshold peak rate occurs at about 150 s^{-1} . The location of the turnover as shown in Figure 5.1 is due

to the combined effect of the background rate and the effective area of the detector. If understood, the turnover can then be extended to smaller peak rates. There is a deviation from the power-law behavior in the form of excess counts in two data points just before the distribution turns over. However, we believe that this is not a result of a real increase in the number of flares. We discuss the possible reasons for this deviation in the next chapter.

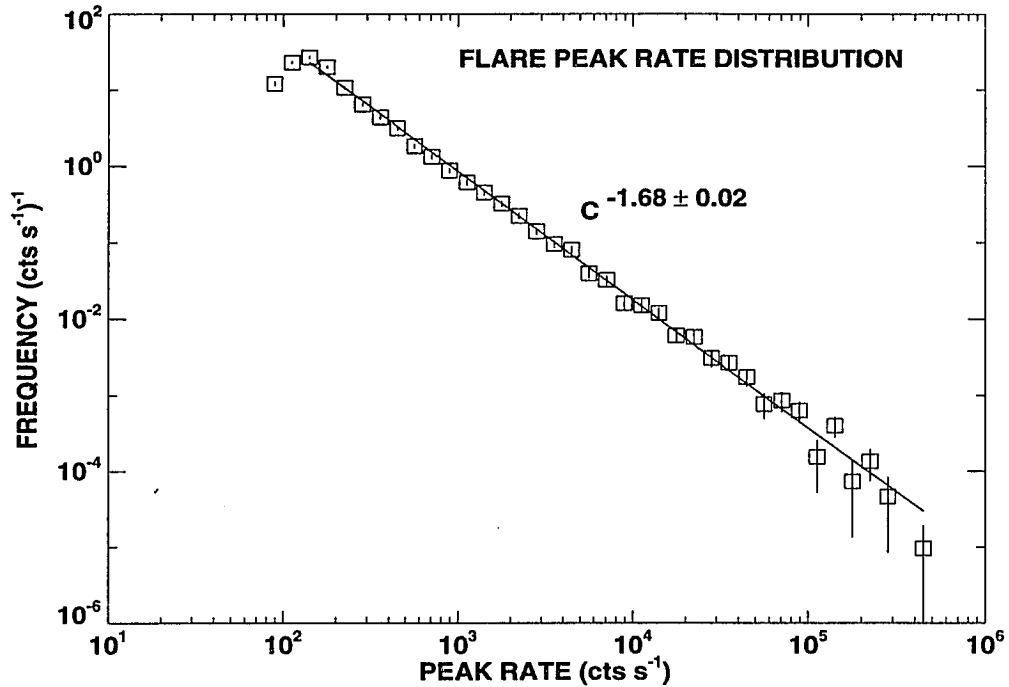


Fig. 5.1. The differential frequency distribution of BATSE flare peak rates assembled from 13 months of observations. The peak rates are normalized to a detector with normal incidence.

Search sensitivity. There are several factors affecting the ability of BATSE to detect small flares. These include a variable background rate (N_b) and a range of detector orientations. The background count rate for the first energy channel varies by as much as 50% from the mean rate. The largest component of background appears to be the diffuse component of the cosmic X-ray flux. We believe this because the background varies with the fraction of the field-of-view (FOV) of each detector that

is filled by the earth, *i.e.*, relatively dark in X-rays. The fraction of the FOV that sees the sky varies throughout the spacecraft orbit. Also, the detector area normal to the solar direction changes frequently because of the Sun's motion across the sky and because of different spacecraft pointings. By selecting data when N_b is low and the angle between the most solar facing detector and the Sun ($\mu \equiv \cos\theta$) is small, the turnover of the distribution is reduced to smaller peak rates, thereby increasing the search sensitivity.

We determine the peak rate limit of our search by looking at how the turnover in the peak flare rate distribution depends on the background rate and detector angle, respectively (Figs. 5.2a and 5.2b). The flares are binned into intervals defined by the background rate. For each background interval, the differential distribution of the flare peak rate is calculated and the turnover in the differential distribution is taken as the size bin with the highest flare frequency.

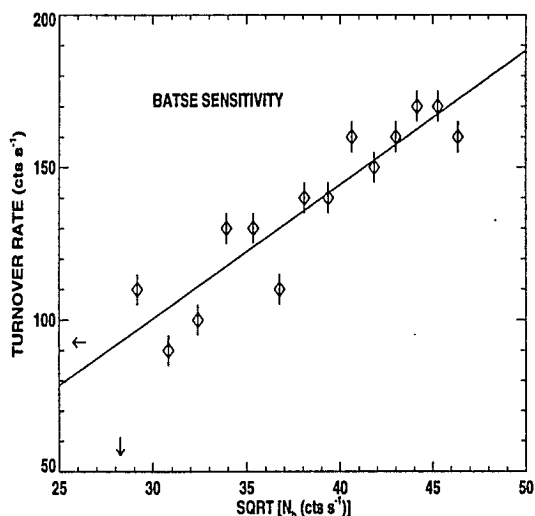


Fig. 5.2a. The turnover in the differential distribution of flare peak rates as a function of flare background rate (N_b). The solid line is a best fit to the data. The arrows indicate the lowest limit observable with BATSE.

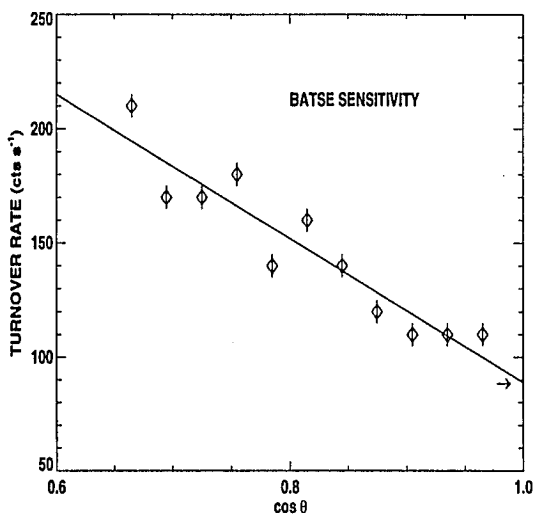


Fig. 5.2b. The turnover in the differential distribution of flare peak rates as a function of $\cos\theta$, where θ is the angle from the Sun to detector normal. The solid line is a best fit to the data. The arrow indicates the lower limit for a detector with normal incidence to the Sun.

Figure 5.2a shows the location of the turnover for each background selected interval. The same analysis is done with solar viewing angle integrated over all background levels (Fig. 5.2b). The smallest achievable BATSE background rates are about $N_b = 800 \text{ s}^{-1}$. This corresponds to a turnover rate of $\sim 90 \text{ s}^{-1}$ (Fig. 5.2a). The best possible case for solar viewing angle is when $\mu = 1$. This corresponds to a turnover rate of again $\sim 90 \text{ s}^{-1}$ representing the smallest flares that can be observed (Fig. 5.2b).

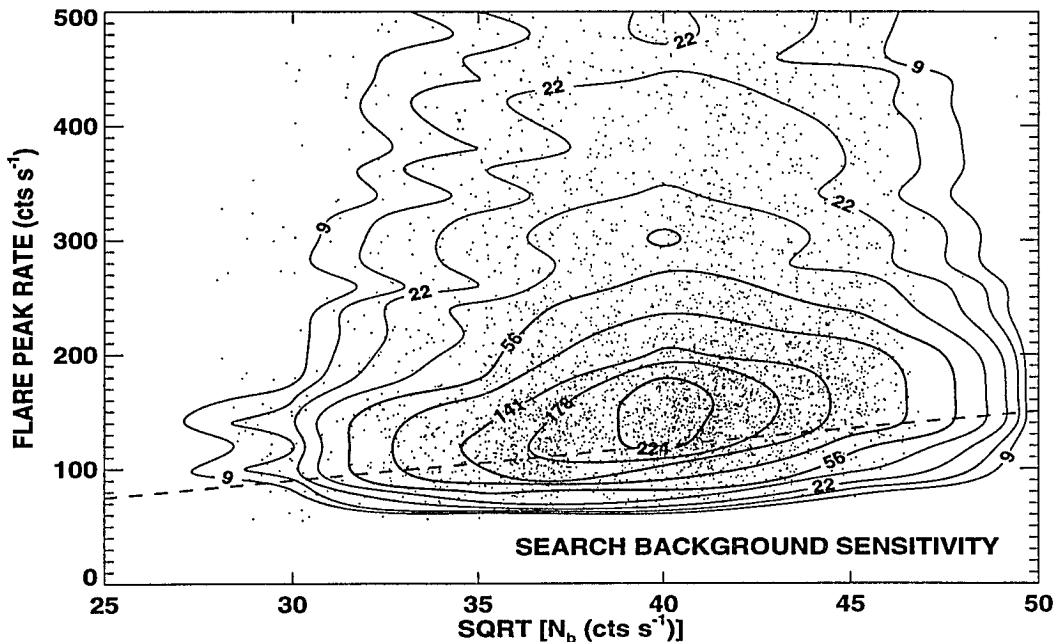


Fig. 5.3. Flares detected with search algorithm as a function of the flare background rate. The contours indicate the density of flares. The dashed-line indicates the peak rate equivalent to a $3\sqrt{N_b}$ detection, illustrating the sensitivity of the search algorithm.

Another way to see how the search routine sensitivity is limited by the detector background rate is to plot the peak flare rate as a function of $\sqrt{N_b}$ for all flares (Fig. 5.3). There is a trend towards lower peak flare rates as the background rate decreases. For a given background rate, the occurrence of flares increases with decreasing peak rate and then drops to zero relatively quickly. The dashed-line (has the equation (peak rate = $3\sqrt{N_b}$)) is intended as a guide showing the threshold, or

turnover, of the distribution and is not a fit. This clearly shows the background limited sensitivity of the search. The points plotted in Fig. 5.2a are equivalent to the location of the maximum flare density for vertical slices of Fig. 5.3.

Best data selection. An ideal selection of only events with $N_b = 800 \text{ s}^{-1}$ and $\mu = 1$ would yield very few events, because of limited observing time under those conditions. Instead, the criteria on N_b and μ are relaxed to $N_b \leq 1250 \text{ s}^{-1}$ and $\mu \geq 0.9$ to provide enough flares to construct a distribution. Plotted in Figure 5.4 is the differential distribution of flare peak rates when the selected flares have the relaxed criteria. The result is that the turnover in the distribution is reduced to $\sim 110 \text{ s}^{-1}$. The data still adhere to a power law down to this value with a best fit index of -1.60 ± 0.18 . Poorer statistics result in larger error bars for these selections. Over 6000 flares are plotted in Figure 5.1 while only 120 flares are plotted in Figure 5.4. The two power-law indices in Figures 5.1 and 5.4 are consistent with one another. More data will reduce the error bars in both cases, but will not extend the distribution to smaller peak rates.

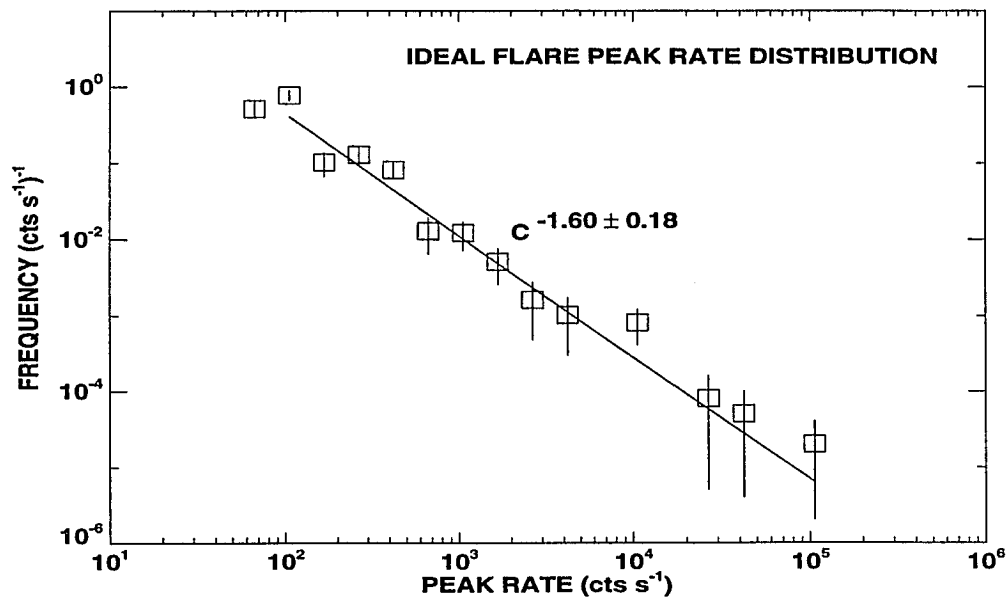


Fig. 5.4. The differential frequency distribution of BATSE flare peak rates for the case of optimal observing conditions ($N_b \leq 1250 \text{ s}^{-1}$ and $\mu \geq 0.90$). The peak rates are normalized to a detector with normal incidence.

The peak photon flux for a given flare is estimated by folding the event count rate through the detector response assuming normal incidence. The flux is calculated assuming that the photon flux of a typical flare is a power-law in energy with a spectral index of $\gamma = -5$. This spectral index is a typical value for small flares (Lin *et al.*, 1984). The peak flux for a 100 s^{-1} event is estimated to be $\sim 0.06 \text{ cm}^{-2} \text{ s}^{-1} \text{ keV}^{-1}$ at 20 keV. We choose this energy because it conforms to earlier analyses (Datlowe *et al.*, 1974; Lin *et al.*, 1984; Dennis, 1985; Crosby *et al.*, 1993). The peak power in the accelerated electrons producing the bremsstrahlung is calculated to be $8 \times 10^{25} \text{ ergs s}^{-1}$, assuming a thick target and a power-law electron energy spectrum.

Variations in Differential Distribution

The sensitivity of BATSE enables us to observe a large number of flares, so that the data can be subdivided in a variety of ways with good statistics. These smaller data sets can represent progressions in time, periods of varying activity level, or any other phenomena that one might expect to affect the distribution of solar flares. We must be careful, though, of effects caused by variations in the background rate, the solar viewing angle, and the solar duty cycle. The first part of this section describes the method used to obtain a data set free of observational bias. The later sections show what was done to search for variations in the differential size distribution power-law index.

Data selection. When we are concerned about the number of flares detected as a function of time the duty cycle must be accounted for (Fig 4.3). This is done through a simple normalization by the fraction of time the Sun was observed.

The variable background rate (N_b) and solar viewing angle (θ) also affect the number of flares observed as a function of time. The goal here is to determine the smallest flares that are observable independent of N_b and μ . From Figs. 5.2a and 5.3 we see that flares with peak rates $\gtrsim 165 \text{ s}^{-1}$ are large enough to be detected with 100% ef-

efficiency even when the background rate is greatest. The solar viewing angle sets a more severe limit on the flares we are able to detect with 100% efficiency. For the data in this work, $0.648 \leq \mu \leq 0.994$. The ability of BATSE to observe a flare of a given flux goes down with decreasing μ , so the limit in this work is set by $\mu = 0.648$. From the linear fit to the data in Fig. 5.2b it is seen that this corresponds to flares with peak rates of 200 s^{-1} . Thus, when we must be careful to use a flare data set not affected by changes in sensitivity only flares with peak rates $\geq 200 \text{ s}^{-1}$ are selected.

The rest of this section is concerned with trying to organize the data in ways that one might reasonably expect to find variations in the power-law index of the differential size distribution. We begin with the best case we can make for variations in the power-law index.

Phase of 51 day period. The daily flare rate data for flares more intense than 200 s^{-1} were epoch-folded with a 51 day period (Figure 5.5). The 51 day period is a harmonic of the fundamental 25.5 day period proposed by Bai and Sturrock (1991). The 51-day period is reported to be in effect throughout the interval covered by the data in this study (Bai, 1994).

The flares were divided into two groups: flares occurring during the maximum of the 51 day phase and flares occurring during the minimum of the 51 day phase. For the flares in each of the groups the differential distribution of flare peak rates is shown in Figure 5.6. The indices of the distributions for flares in the maximum phase are -1.65 ± 0.03 and -1.74 ± 0.04 for the minimum phase. The difference in the indices is 0.09 ± 0.05 . This difference, while not conclusive, is the only significant result that was found for the variation of the power-law index of the differential distribution of peak rates. The two distributions are normalized to have equal numbers of flares and the χ^2 statistic is calculated to test the hypothesis that the slopes of the two distributions are consistent.

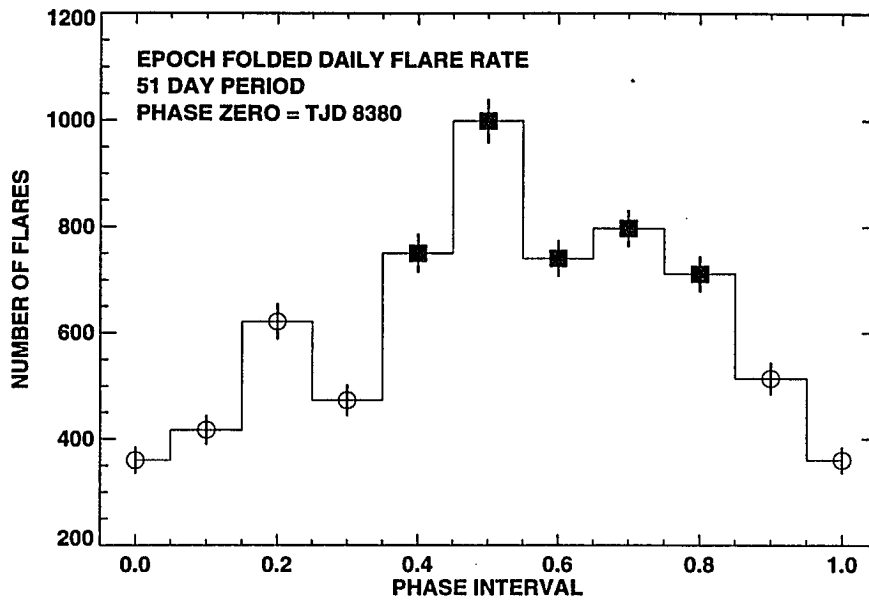


Fig. 5.5. The 51 day epoch-folded daily flare rate. Filled squares indicate the peak of the 51 day period, open circles indicate the minimum of the period. The phase is chosen to match Bai (1994).

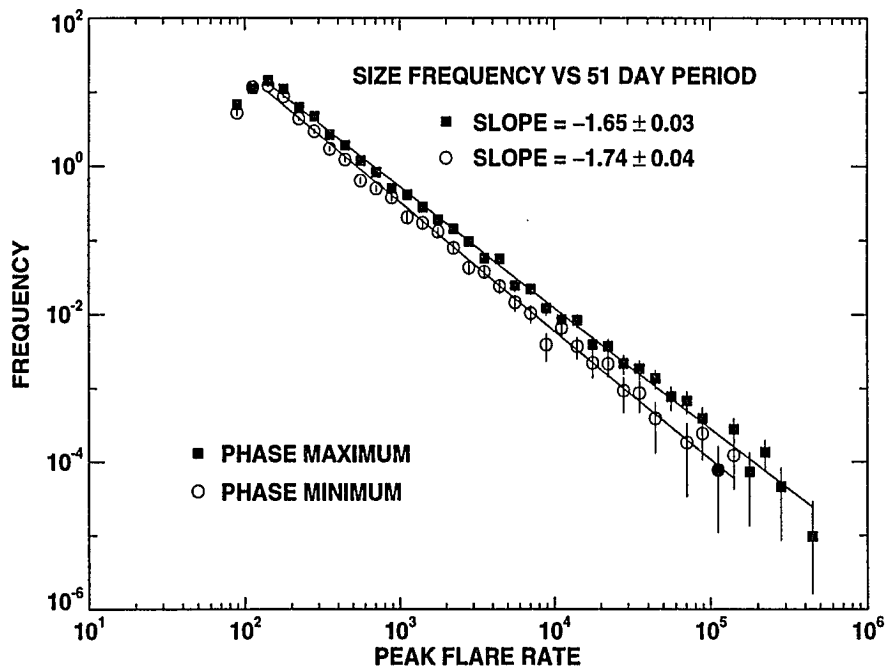


Fig. 5.6. Differential distribution of flare peak rates for the maximum and minimum phases of a 51 day period.

We find that $\chi^2 = 22$ with 23 degrees of freedom. There is a 52% probability that the two data sets are drawn from the same population. It is possible that small flares are undercounted during periods when there are many large flares. The small flares may not be observable due to the high count rates produced by large flares. This would result in a flattening of the size frequency distribution during periods of activity with many large flares.

Variations with activity. It may be that the Sun preferentially produces flares of a certain size on days when it is more or less active. We searched for variations in the power-law index as a function of flare activity in two additional ways. We measure the level of flaring activity by the number of flares observed.

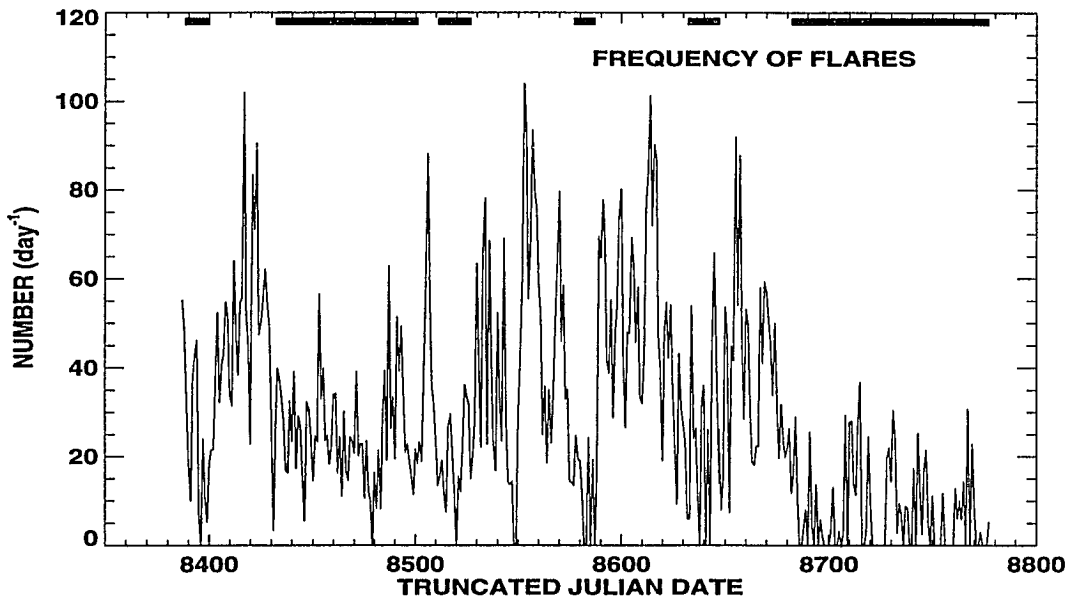


Fig. 5.7. The flare frequency per day corrected for the BATSE duty cycle. Dark shading indicates periods of low activity.

First, inspired by the previous result which rigidly organized the data into periods of high and low activity defined by a 51 day period, we instead subjectively chose periods of high and low activity (Fig. 5.7). The periods of low activity are indicated by dark shading at the top of Figure 5.7. The differential size distribution of flares from low activity and high activity periods are plotted (Figs. 5.8a and 5.8b). The

best fit power-law spectral indices obtained were -1.71 ± 0.04 for low activity flares and -1.68 ± 0.02 for high activity flares. There is no indication that the spectral index of the differential size distribution changes with activity levels when organized in this arbitrary way.

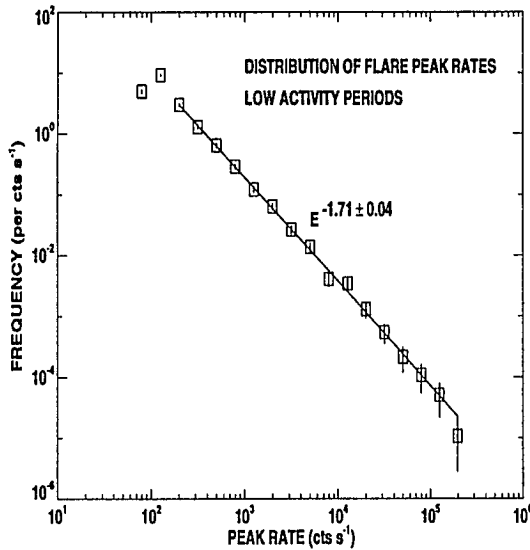


Fig. 5.8a. The differential distribution of flare peak rates for flares occurring during periods of low activity.

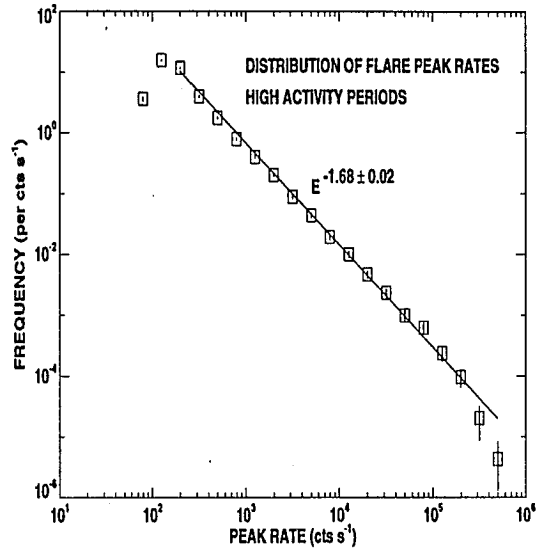


Fig. 5.8b. The differential distribution of flare peak rates for flares occurring during periods of high activity.

Second, we binned the data into time intervals of 27 and 25.5 days, and multiples thereof. These intervals correspond to the average solar rotation period and to the possible fundamental period in solar flare occurrence rate respectively (Bai and Sturrock 1991). The data can be divided into fourteen 27 day intervals and fifteen 25.5 day intervals data. For the flares in each interval, the differential distribution of flare peak rates was plotted. Each distribution was fit with a power-law and the best fit power-law index was obtained.

The power-law index for each of the intervals is plotted versus the number of flares in the interval in order to reveal any dependence of the power-law spectral index on activity level (Figs. 5.9a and 5.9b). The power-law indices as a function of activity level were examined for trends by use of a linear fit. The best fit slopes in Figs. 5.9a

and 5.9b are $(-7.9 \pm 10.0) \times 10^{-5}/27$ days and $(-1.7 \pm 1.2) \times 10^{-4}/25.5$ days. The straight line fits are consistent with no variation in the power-law index of the differential distribution of flare peak rates with flare activity.

Binning the data into longer intervals may reveal any variation with time not now apparent because of the limited statistics. The same analysis was carried out for intervals of size 51 (25.5×2), 54 (27×2), and 76.5 (25.5×3) days. This differs from the epoch-folding case in that information about time evolution is retained here. In all cases, there was no evident trend.

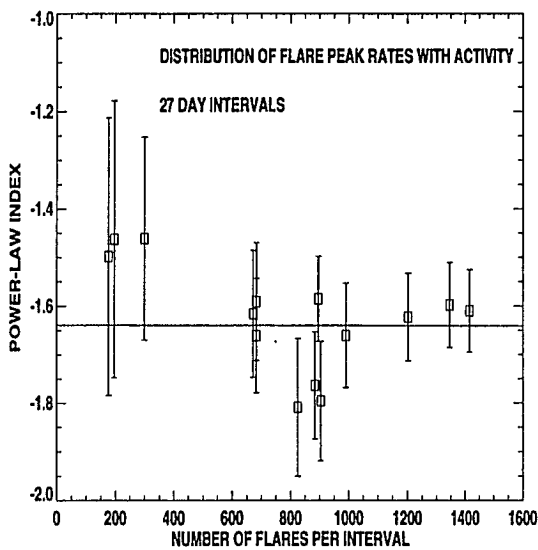


Fig. 5.9a. Slope of the differential distribution of flare peak rates as a function of the flaring rate. Each time interval is 27 days in size. The data are fit with a straight line.

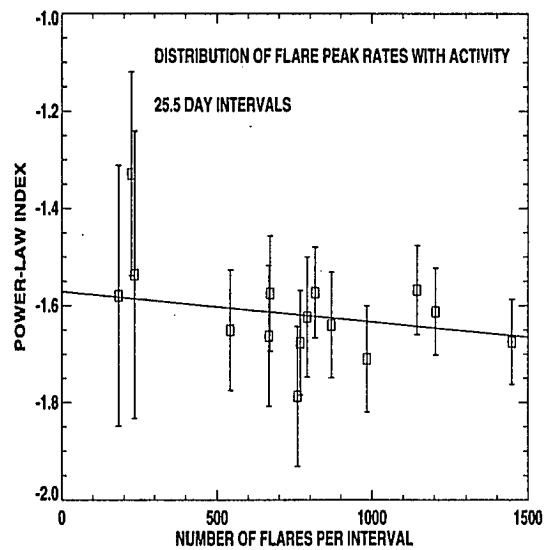


Fig. 5.9b. Slope of the differential distribution of flare peak rates as a function of the flaring rate. Each time interval is 25.5 days in size. The data are fit with a straight line.

Trend over experiment duration. We also might expect that the power-law index of the flare size distribution varies with time. We searched for evidence of any trends with time in the power-law index.

Utilizing the data binned into intervals of 27 and 25.5 days in the previous section we examined how the power-law index varied over the duration of this study. The power-law indices found for the flares in each interval are plotted against time instead

of activity level (Figs. 5.10a and 5.10b). The data in each figure are fit with a straight line. The slopes of the best fit lines are $(-2.3 \pm 9.3) \times 10^{-3}/27$ days and $(-8.8 \pm 8.9) \times 10^{-3}/25.5$ days. The data are consistent with a constant power-law index. As before, binning the data into longer intervals may reveal any variation with time not now apparent because of the limited statistics. Similar analyses were carried out for intervals of size 51 (25.5×2), 54 (27×2), and 76.5 (25.5×3) days. In all cases, the power-law index of the differential distribution of peak flare rates does not show a consistent trend for changes in time. More data are needed to search for a slowly varying power-law index.

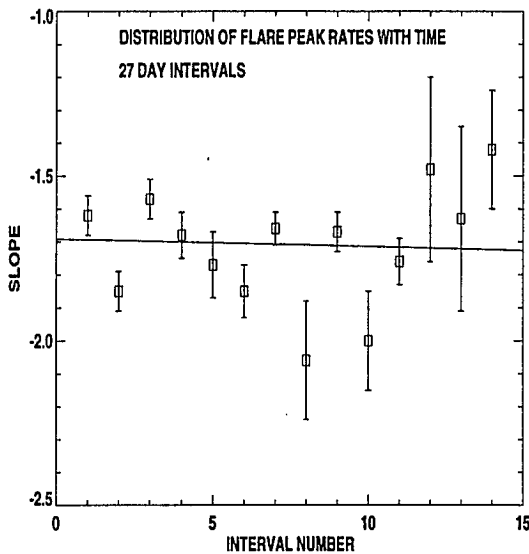


Fig. 5.10a. Slope of the differential distribution of flare peak rates as a function of time. Each time interval is 27 days. The data are fit with a straight line.

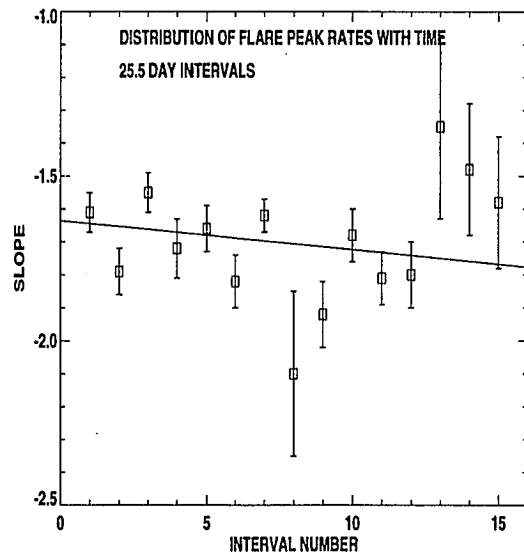


Fig. 5.10b. Slope of the differential distribution of flare peak rates as a function of time. Each time interval is 25.5 days. The data are fit with a straight line.

Time Series Analyses

The possible existence of periodic behavior in solar flare occurrence data leads us to question whether there is any periodic behavior evident in the BATSE data. A 51 day period is reported to be operating during the time interval of this study (Bai,

1994). We should see evidence of the 154 day period that was discovered during the last solar cycle, if it is operating during the current solar cycle (Rieger, *et al.*, 1984). Also, there is evidence that the flare size frequency distribution power-law index is variable, so one might expect that flares of certain sizes may occur preferentially at times (Bai, 1993; Kucera, 1994). The 51 day period was found for large GOES flares (class \geq M3.0). We want to determine if this period exists for flares of all sizes. If flares of certain sizes occur preferentially, we want to determine when they occur and for how long.

Time series analysis is performed in two ways. The first part of this section shows the results obtained from an autocorrelation of the daily flare rates. The second part shows the results of performing a wavelet analysis on the daily flare rate.

Autocorrelation of the Flare Frequency

Autocorrelations of the daily flare occurrence rate are used to identify periods present in the data. The small data set being used precludes definitive conclusions from being made about the existence of periods longer than about 40 days (periods with at least ten cycles). It is, however, possible to search for differences in the autocorrelation results as a function of flare size for all periods, including those > 40 days. The flares with peak rates $C_p > 200 \text{ s}^{-1}$ were divided into three groups: small flares ($200 \text{ s}^{-1} < C_p < 351 \text{ s}^{-1}$), intermediate size flares ($351 \text{ s}^{-1} \leq C_p < 1035 \text{ s}^{-1}$), and large flares ($1035 \text{ s}^{-1} \leq C_p$). The C_p divisions were made so that each group has an equal number of flares (~ 1200). The flare frequency for each group is plotted in Figures 5.11a–c.

The autocorrelation function used to search for periodic behavior in the daily flare occurrence rate data is

$$A_\tau = \frac{\sum_{i=0}^{N-\tau} (N_i N_{i+\tau})}{\sum_{i=0}^{N-\tau} (N_i N_i)} . \quad (5.1)$$

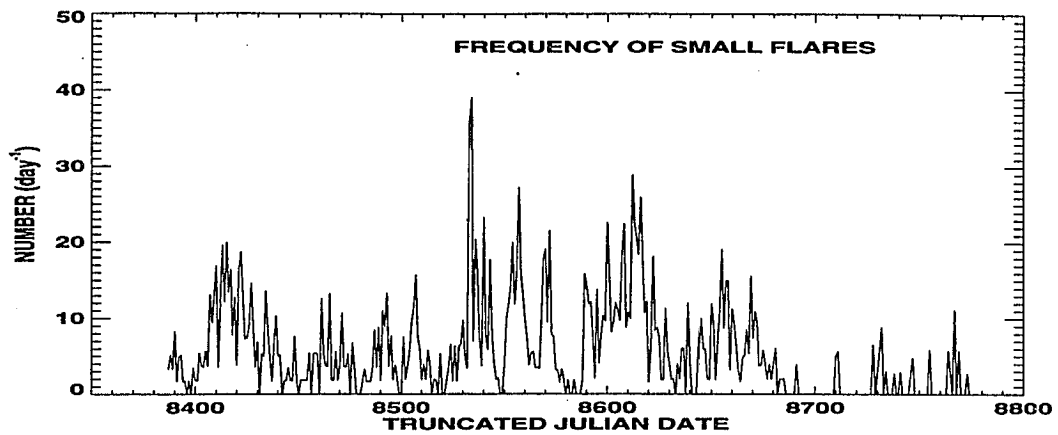


Figure 9a

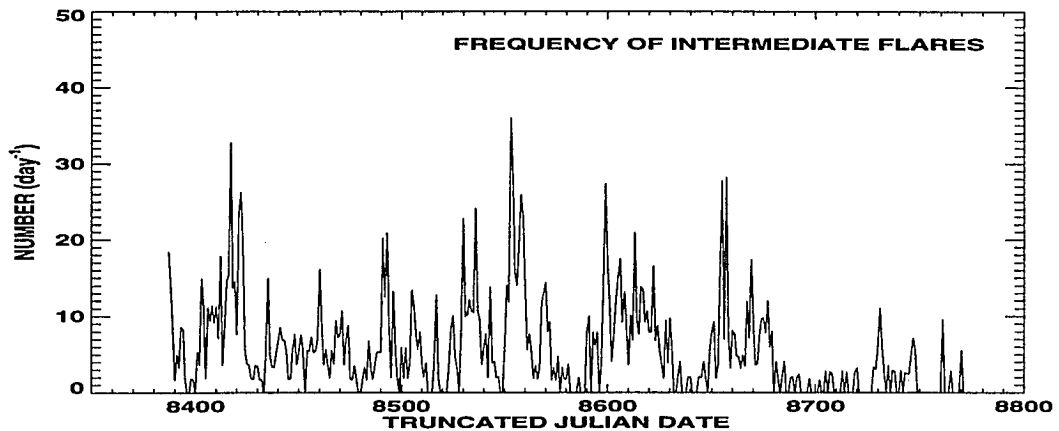


Figure 9b

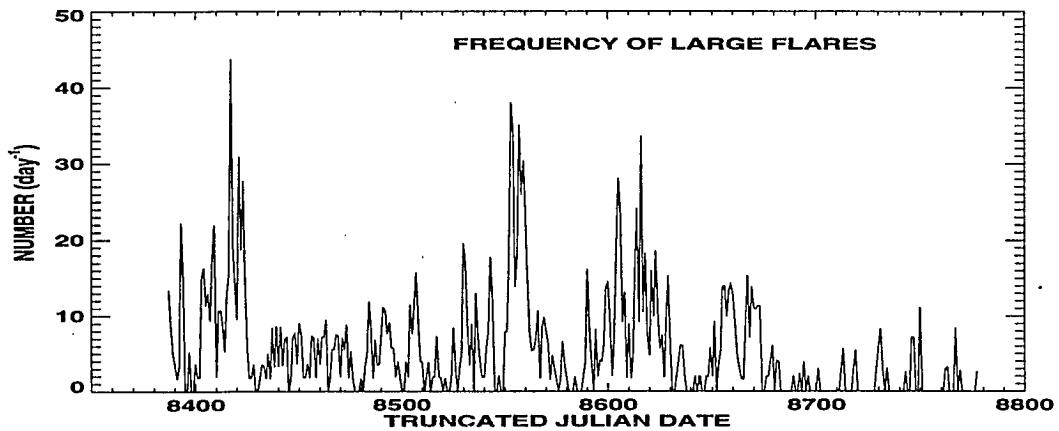


Figure 9c

Fig. 5.11. (a) Flare frequency per day corrected for duty cycle for $200 \text{ s}^{-1} < C_p < 351 \text{ s}^{-1}$. (b) $351 \text{ s}^{-1} \leq C_p < 1035 \text{ s}^{-1}$. (c) $1035 \text{ s}^{-1} \leq C_p$.

The autocorrelation was evaluated for periods (τ) from 0 to 195 days (1/2 of total survey). The results of the autocorrelation analysis are plotted in Figures 5.12a-c.

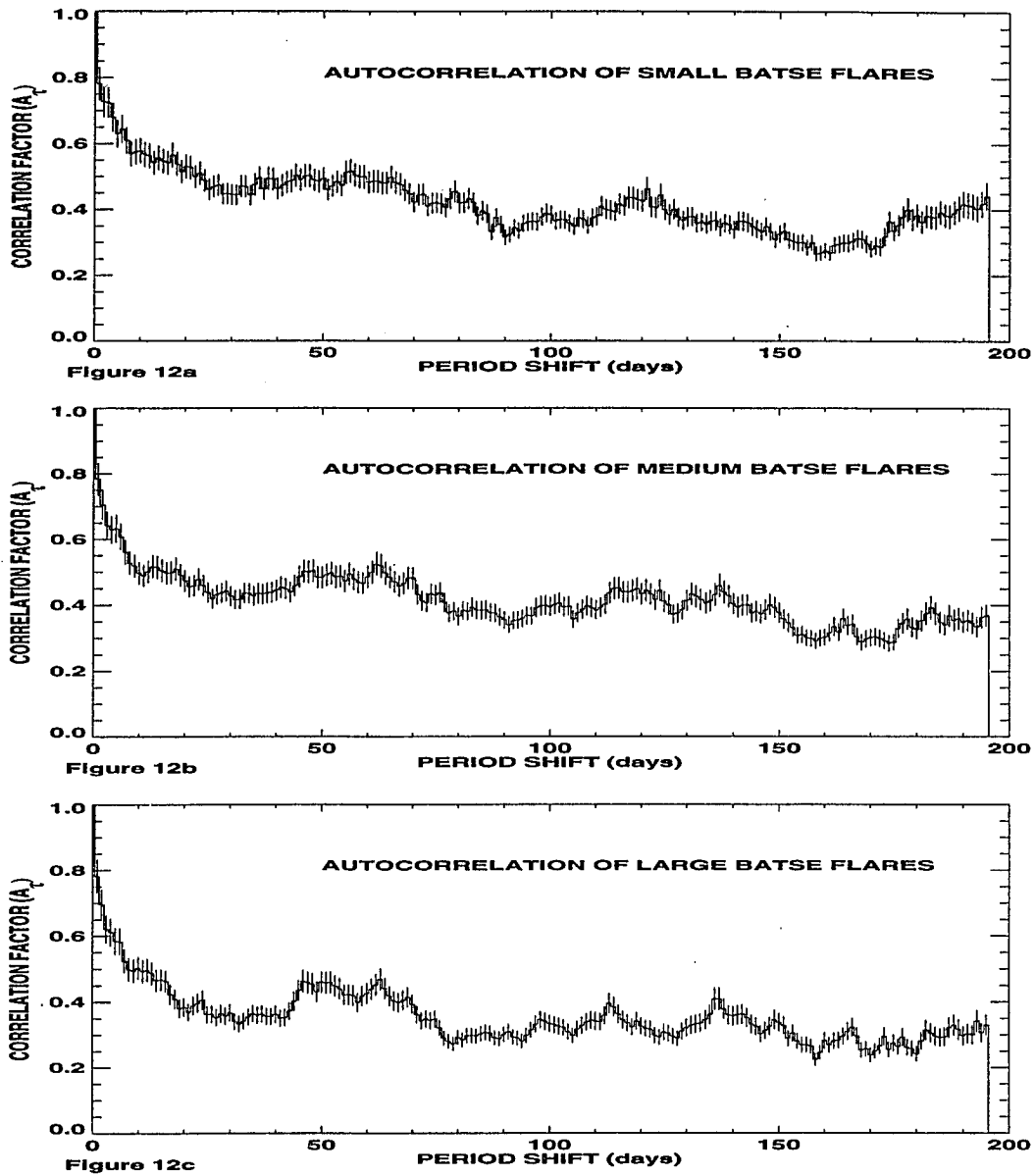


Fig. 5.12. (a) Autocorrelation of daily flare rates for $200 \text{ s}^{-1} < C_p < 351 \text{ s}^{-1}$. (b) $351 \text{ s}^{-1} \leq C_p < 1035 \text{ s}^{-1}$. (c) $1035 \text{ s}^{-1} \leq C_p$.

The autocorrelation, as expected, drops off rapidly for very short periods and then declines slowly beyond periods of about 7–8 days. The rapid initial drop is an indication that flare activity stays at constant levels for only a few days. The autocorrelation of small flares is otherwise relatively featureless. However, in comparing the correlations of the intermediate and large flares to the small flares, we see some

differences. For large flares, the autocorrelation is significantly greater in the range of $\tau = 45$ to 65 days than it is at 40 or 75 days. In the case of intermediate size flares, there is some evidence that a similar bump occurs. The small flares show little evidence of the feature. This indicates that the 51 day period found for large GOES flares also exists in the BATSE data (as the 51 day epoch-folded data told us) but apparently only for large flares. There is no evidence for the period of 154 days found during the previous solar cycle. There is also no evidence of the fundamental 25.5 day period (Bai and Sturrock, 1991) and the only harmonic observed is at 51 days. The broadness of the feature at 51 days and the lack of visible harmonics indicates that it is at best quasi-periodic.

Wavelet Analysis of the Flare Frequency

We use wavelet analysis in order to determine the time scales (levels) over which flare activity is occurring in the BATSE daily flare rate. The wavelet analysis differs from the autocorrelation analysis in that it identifies the frequencies associated with structures in the data, where the autocorrelation analysis measures the time between structures.

Fourier analysis can show if a particular frequency is present in the signal, but if the frequency is short-lived, it cannot show where in the time series the frequency existed. Wavelet analysis not only breaks a signal into frequency components, but it shows when in time the frequency components arise (Hunt *et al.*, 1993; Newland, 1993). We performed a wavelet analysis on the same three data sets as in the autocorrelation analysis.

In wavelet analysis, the goal is to decompose an input signal $f(x)$ of length T into an infinite sum of wavelets (W) of different levels (Eq. 5.2).

$$f(x) = \sum_{j=-\infty}^{\infty} \sum_{k=-\infty}^{\infty} c_{j,k} W(2^j x - \frac{k}{T}), \text{ where} \quad (5.2)$$

$x \equiv \frac{t}{T}$ is a non-dimensional variable ($0 \leq x \leq 1$) and j is the wavelet level.

The Haar wavelet, which forms an orthonormal basis, is used here because of its simplicity (Eq. 5.3).

$$W(z) = \begin{cases} -1 & 0 \leq z < \frac{1}{2} \\ 1 & \frac{1}{2} \leq z < 1 \\ 0 & \text{otherwise.} \end{cases} \quad (5.3)$$

The Haar wavelet is plotted for levels $-1, 0, 1, 2, 3,$ and 4 (Fig. 5.13).

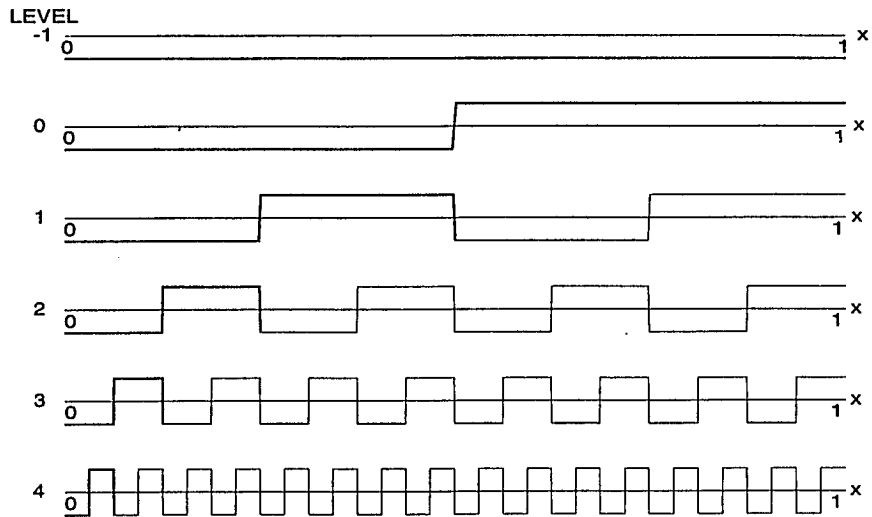


Fig. 5.13. Haar wavelets with unit amplitude for levels $-1, 0, 1, 2, 3,$ and 4 ; for these levels there are $1/2, 1, 2, 4, 8,$ and 16 wavelets per unit interval x . The elementary wavelet is highlighted.

The total length of the data determines how many levels are necessary for the analysis. The number of levels n is given by $T = 2^{n-1}$, where T is the number of points in the data set. In this case, the 391 days of data are padded with zeroes to make 512 data points for 10 time scales. The highest level, or smallest features, that can be measured corresponds to twice the interval spacing size of the data, *i.e.* two days. The only values of j which contribute to the sum in Eq. 5.2 are $-1 \leq j \leq n$, as higher levels would sample the data on a scale finer than the resolution of the data. The first two levels, -1 and 0 correspond to DC and AC normalizations of the data. The “frequency” being measured doubles with each increasing scale.

Plotted in Figure 5.14 is the result of applying wavelet analysis to the frequency distribution of all BATSE flares with peak rates $\geq 200 \text{ s}^{-1}$. The plot, known as

a mean square map (conceptually related to power in a Fourier spectrum), is the wavelet amplitude squared plotted versus level and time. The lightest shades indicate where the amplitude, or power, of the wavelet is greatest. Dark areas indicate no power. Levels 0 and 1 are the DC and AC normalizations and level 9 corresponds to a frequency of 2 days (note the two lowest levels are now designated 0 and 1).

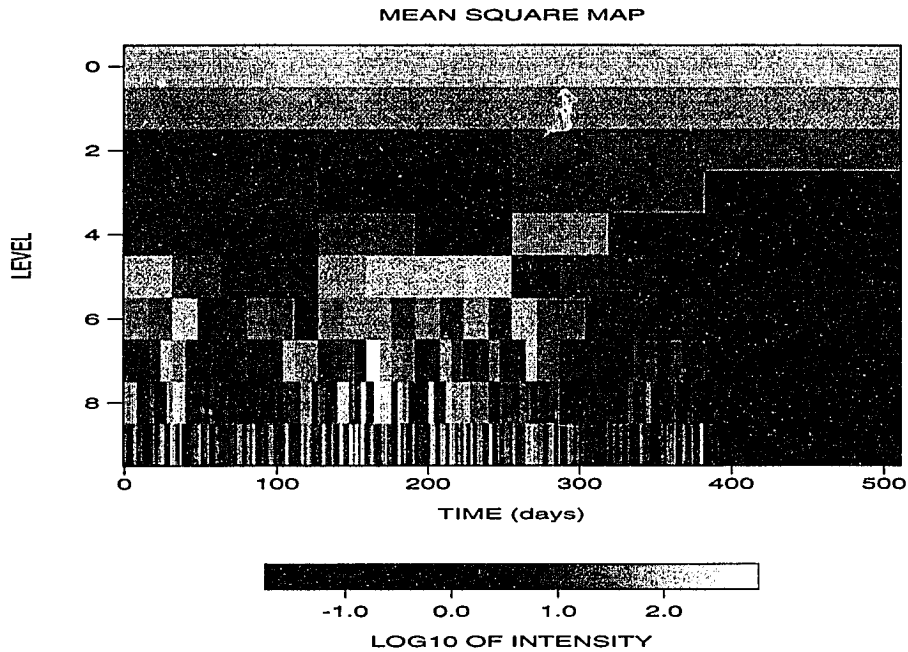


Fig. 5.14. The mean square map for all BATSE flares with peak rate $\geq 200 \text{ s}^{-1}$.

It is not immediately clear what can be obtained from the mean square map. However, if the mean square map is integrated over all times for each of the three data sets one gets the results seen in Figures 5.15a, b, and c, which essentially reproduce what one would obtain from Fourier analysis of the data.

The time integrated mean square maps show that there is little power in the daily flare rate at long time scales. The power in the daily flare rate shows an increase at time scales of 32 days (level 5) and remains high for shorter time scales. This indicates that flare activity generally lasts for time scales of 32_{-8}^{+16} days maximum, independent of flare size. A single active region would only produce flare activity we can see for

~ 14 days. Two active regions 180° apart could easily give activity lasting 32 days, but the active regions could only produce flares for a maximum of 32 days.

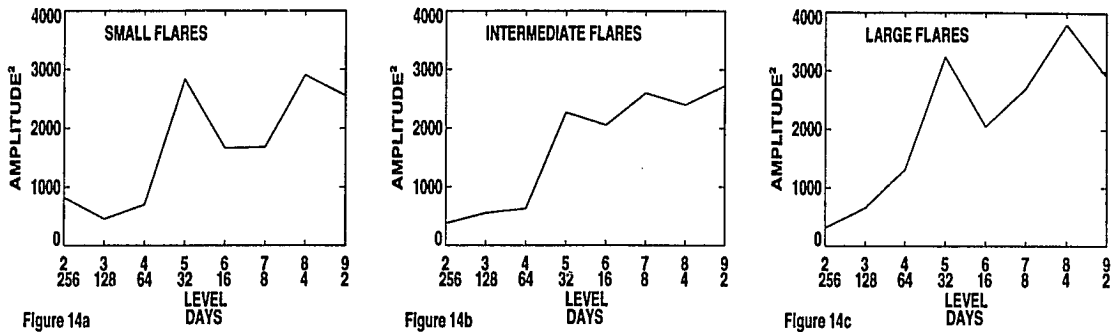


Fig. 5.15. (a) The time integrated mean square map for small flares. (b) Time integrated mean square map for intermediate flares. (c) Time integrated mean square map for large flares.

Since the signal increases in size at level 5 we plot its power as a function of time (Figs. 5.16a-c). The epochs (32 days wide) where the power in level 5 is high can then be associated with structures in the daily flare frequency. The power in level 5 appears to come in impulsive bursts which are sometimes resolvable, corresponding to active periods of size ~ 1 solar rotation. Examples of these ~ 32 day structures begin at TJDs 8400, 8550, and 8600.

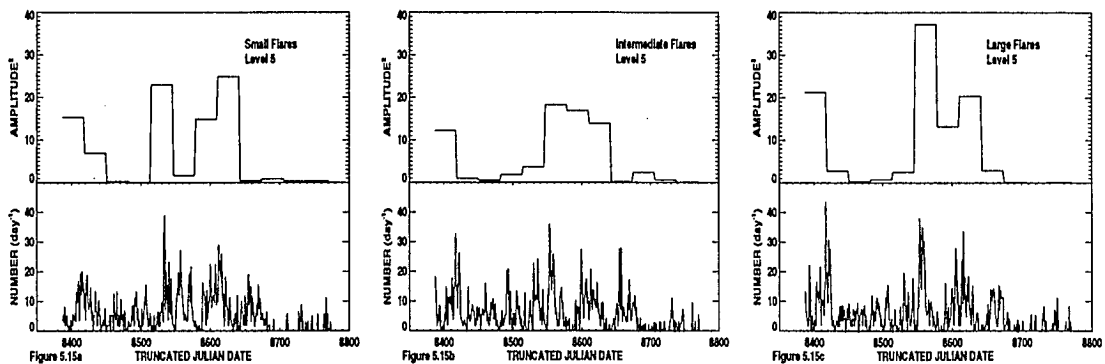


Fig. 5.16. The square of the wavelet amplitude at level 5 for small flares (a). The square of the wavelet amplitude at level 5 for intermediate sized flares (b). The square of the wavelet amplitude at level 5 for large flares (c). The corresponding flare frequency data are included in each figure for reference.

Time Distribution of Solar Flares

Sympathetic flaring, where flares are triggered by a disturbance caused by a previously occurring flare has been reported (Richardson, 1936, 1951; Becker, 1958; Smith and Harvey, 1971; Simnett, 1974; Gergeley and Erickson, 1975). It is not known what fraction of flares may be a result of such a disturbance. Sympathetic flaring may be a result of particles propagating to another site via direct magnetic connections (Simnett, 1974) or because waves, such as Moreton waves, produced at one site propagate to another site, triggering a flare (Richardson, 1936, 1951; Becker, 1958; Smith and Harvey, 1971; Gergeley and Erickson, 1975). Skylab observations of interconnected X-ray loops found no evidence of sympathetic flares (Fritzová-Svestková and Chase, 1975; Chase *et al.*, 1976). However, YOHKOH observations show that active regions interact with each other through magnetic connections as seen in X-rays of ~ 1 keV (Strong, 1994).

Statistical studies of the time of occurrence of solar flares have been divided according to whether flares occur sympathetically (Richardson, 1951; Waldmeier, 1938; Smith and Smith, 1963; Gergeley and Erickson, 1975).

We consider the sympathetic nature of flare occurrence by testing the null hypothesis that flares observed by BATSE are randomly distributed in time. Furthermore, we can investigate whether the size of events is affected by the time between events, or conversely, whether the size of an event affects the ability of an active region to trigger other flares. We test two flare occurrence models with this analysis (Rosner and Vaiana, 1978; Lu and Hamilton, 1991). Most previous studies of the sympathetic nature of flares have been of larger, optical flares. This study adds smaller flares to the analysis which means that we have a more complete flare sample than earlier studies, thus we will see more of the total energy released and that may help to clear the picture. However, the 2 minute time lag between events that the automated search routine requires limits the ability to test sympathetic flaring to only

sympathetic events triggered by slowly propagating disturbances.

Randomness of flare occurrence. We consider the hypothesis that flares are randomly distributed in time. The frequency of times between consecutive flares is plotted for all flares between TJDs 8387 (11 May 91) and 8690 (09 Mar 92) with $C_p > 200 \text{ s}^{-1}$ (Fig. 5.17). The restriction on peak rates is used to ensure that we have a complete sample for all flare sizes included. The restriction on TJDs is intended to avoid data affected by the tape recorder failure. Also, time intervals less than two minutes are excluded to account for the two minute lag time introduced in the search algorithm.

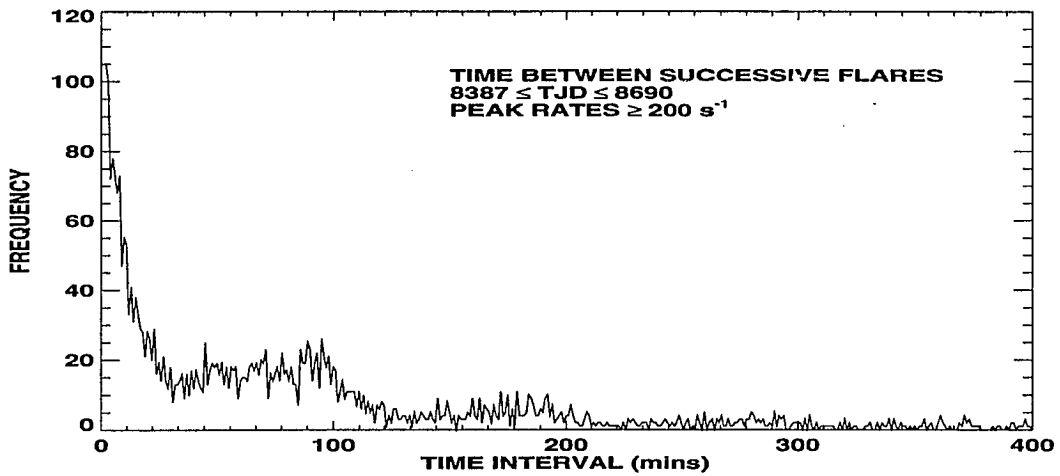


Fig. 5.17. The distribution of times between successive BATSE flares with peak rates $>200 \text{ s}^{-1}$.

If we assume that flaring is a stochastic process and if flaring regions are isolated from each other and if the duration of flares is small compared to the mean time between flares, then the flare occurrence can be described as a Poisson probability distribution (Eq. 5.4).

$$P(n, t) = \frac{(\lambda t)^n}{n!} e^{-\lambda t}, \text{ where} \quad (5.4)$$

$P(n, t)$ is the probability of observing n flares in time t and λ is the mean flare rate. It can be shown that the distribution of time intervals between events which are Poisson

distributed is

$$P(\Delta) = \lambda e^{-\lambda t} . \quad (5.5)$$

It is clear that the distribution of times between BATSE flares cannot be fit by a single exponential (Fig. 5.17). However, the distribution of time between flares is biased because flares are not seen during earth occultations and SAA passages.

In order to understand the data in Fig. 5.17 we performed a Monte Carlo simulation to test the null hypothesis that flaring is a random process. A timeline for solar viewing by the BATSE instrument was constructed including the times of SAA passage and earth occultation. The Monte Carlo simulation proceeds by randomly dropping events onto the timeline and then calculating the distribution of times between events.

The BATSE timeline is constructed for days TJD= 8387 through TJD= 8690, which does not include the period of the tape recorder failure. There were 3550 flares observed in the interval and the true flare count is 6596 when corrected for the BATSE duty cycle. However, the true flare rate is not a constant. The flare rate (λ) is highly variable, ranging from zero to $>100 \text{ day}^{-1}$. To reproduce the variability in λ , days with similar number of flares are grouped together and a distribution of average flare rates λ_i is calculated. Events are then randomly dropped onto the timeline, but with the requirement that the distribution of flare rates is preserved. The average flare rate is calculated over short intervals for times of high activity because they dominate the exponential $e^{-\lambda t}$ for small values of t and because highly productive active regions show the most rapid variability.

When all of the flares have been randomly distributed onto the BATSE timeline, we compute the distribution of time between events with the assumption that the Sun is always visible (*i.e.* no SAA passage or earth occultations). The resulting distribution is a sum of exponentials with mean flare rates λ_i (Eq. 5.2 and Fig. 5.18).

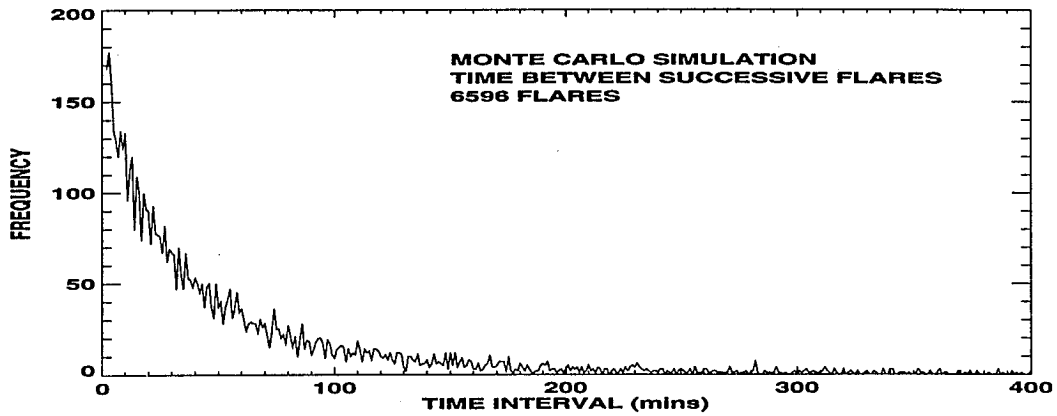


Fig. 5.18. The distribution of times between successive simulated flares from the BATSE timeline with the assumption that the Sun is visible during SAA passage and earth occultation.

If flares that are randomly distributed occur during a time of SAA passage or earth occultation they would not be detected and thus in our simulation these events should not be included. The distribution of times between flares, when flares that occur during SAA passage and earth occultation are excluded is plotted in Fig. 5.19. The simulated distribution agrees with the real one (compare Figs. 5.17 and 5.19). The difference in the time between BATSE flares (Fig. 5.17) and the simulated flares (Fig. 5.19) is plotted in Fig. 5.20.

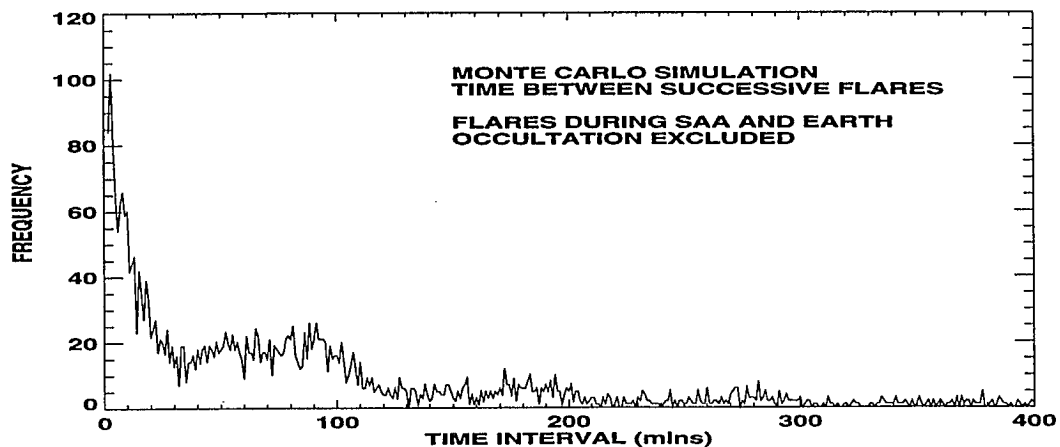


Fig. 5.19. The distribution of times between successive simulated flares from the BATSE timeline with flares occurring during SAA passage and earth occultation excluded.

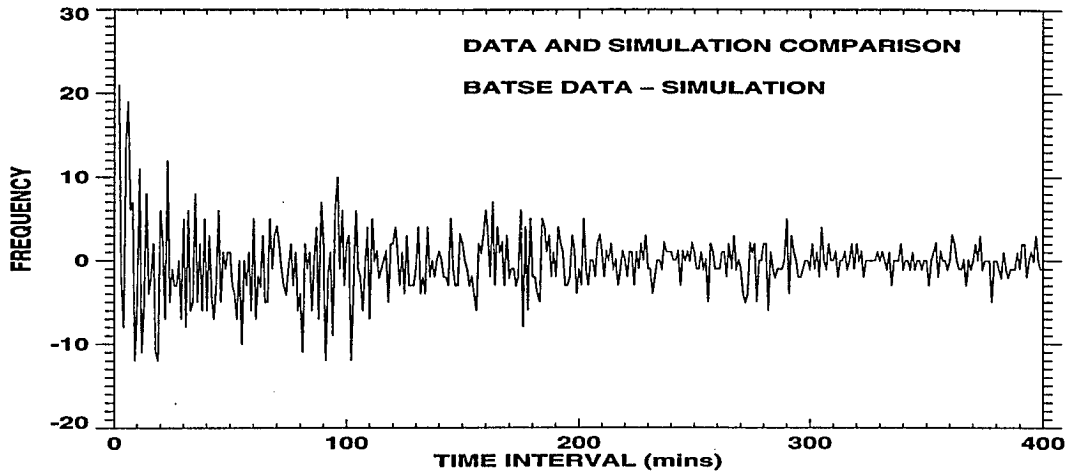


Fig. 5.20. Comparison of the distribution of times between simulated randomly distributed flares and successive BATSE flares. This is the result of subtracting Fig. 5.18 from Fig. 5.16.

We compute χ^2 to determine the probability that the null hypothesis is true. We obtain a value of $\chi^2 = 97.4$ for 119 degrees of freedom. There is a 93% probability that the two distributions are equivalent. We compared the two datasets over a range that extends up to only 120 minutes between flares, where the number of events in each bin is ≥ 10 . In fact, 120 minutes may be a reasonable time over which to compare the distributions. For sympathetic flaring to occur there must be a physical connection between the two flares. The physical connection might be a wave created by the first flare. A slowly traveling wave, traveling at the sound speed, might cross the solar surface at about 300 km s^{-1} and would take about 2 hrs to cross the Sun.

We test our ability to detect sympathetic flaring by performing the same Monte Carlo analysis, except now some fraction of the events are assumed to be sympathetic, occurring within some determined time of a previous flare. The distribution of times δ between the initial flare and the sympathetic flare is assumed to be an exponential with a time constant τ

$$\delta(t) = A \exp(-t/\tau) , \quad (5.6)$$

where A is the fraction of events that occur sympathetically. The primary events are

again distributed randomly as before, except additionally the appropriate fraction of these events (A) are distributed according to Eq. 5.6. That is, a random event is chosen and the sympathetic flare is placed at a time t later by choosing a deviate from an exponential distribution with time constant τ . We ran the Monte Carlo simulation for a range of A and τ . Each simulation is tested against the data and the probability is computed that the simulation and the data derive from different parent populations. The resulting probabilities are plotted in Fig. 5.21.

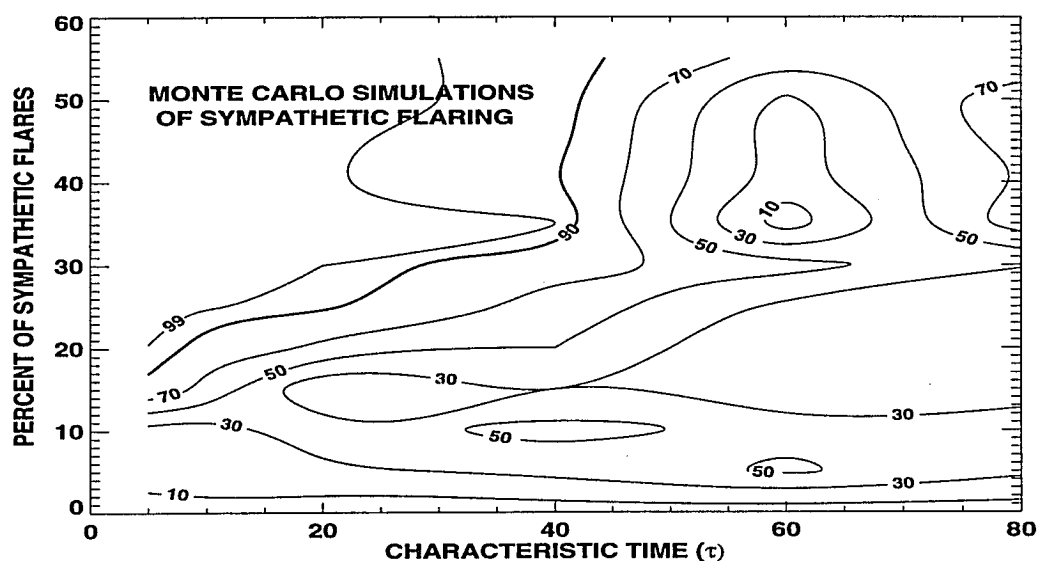


Fig. 5.21. Monte Carlo simulations of sympathetic flaring. The probability that the simulated sympathetic flare distributions and the BATSE data are not drawn from the same distribution is plotted. We consider the distributions to be different when the probability is greater than 90%.

We find that we cannot exclude sympathetic flaring if fewer than ~ 20 - 30% of the flares occur sympathetically, at least for sympathetic flaring occurring with characteristic times greater than 2 minutes and less than 40 minutes. For the simulations where the characteristic time for sympathetic flaring is > 40 minutes, we find that the simulated sympathetic flaring cases are consistent with the BATSE data for all cases tested. We believe that when the characteristic time exceeds 40 minutes

it approaches the average rate of flaring observed with BATSE and thus the BATSE data and the sympathetic data are both from similar distributions.

Flare size dependence. Also of interest is whether there is a correlation between the size of flares and the time between them. For example, if there is a finite amount of free energy available for flaring, and this free energy can only be replenished slowly, then after a large flare occurs one would not expect another large flare to occur soon thereafter. We test the hypothesis that there is no correlation between the size of a flare and the time until the next flare by considering the percentage of events greater than a given size in each time bin of Fig. 5.17.

We divide the flares into size groups similar to before, considering the percentage of flares with $C_p \geq 351 \text{ s}^{-1}$ and with $C_p \geq 1035 \text{ s}^{-1}$ in each delta time bin. The flares with $C_p \geq 351 \text{ s}^{-1}$ constitute 2/3 of all flares, so they should constitute 2/3 of the flares in each time bin for the null hypothesis to be true. The flares with peak rates $\geq 1035 \text{ s}^{-1}$ constitute 1/3 of all flares, so they should constitute 1/3 of the flares of each individual time bin. The percentage of flares in each time interval bin that are $\geq 351 \text{ s}^{-1}$ and that are $\geq 1035 \text{ s}^{-1}$ is plotted (Figs. 5.22a and b). Since we know what the expected number of flares is in each bin, we can calculate the χ^2 statistic to compare the expected and actual values. For the case of peak rates $\geq 351 \text{ s}^{-1}$, the probability that the time between two flares depends on the size of the first flare is $< 1\%$. The probability that the time between two flares depends on the size of the first flare is $< 1\%$ for the case where the first flare is larger than 1035 s^{-1} .

We find little evidence that the occurrence of a flare is likely to trigger another event. No greater than about 25% of all flares could be a result of sympathetic flaring, according to our results. Otherwise, we would see evidence for a non-random nature of flare occurrence. Events must be separated by at least two minutes. The time of flare occurrence is described by a Poisson probability distribution with no greater than 25% of the flares being a result of sympathetic flaring. We also find no evidence

for a correlation between the size of flares and the time between successive flares.

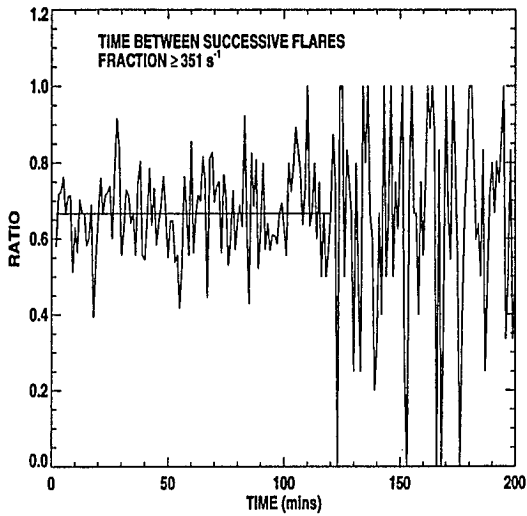


Fig. 5.22a. The percentage of flares with peak rates $\geq 351 \text{ s}^{-1}$ as a function of time after the occurrence of the flare until the next flare. We expect $2/3$ of the flares in each bin to be $\geq 351 \text{ s}^{-1}$ and the fit to the data confirms that.

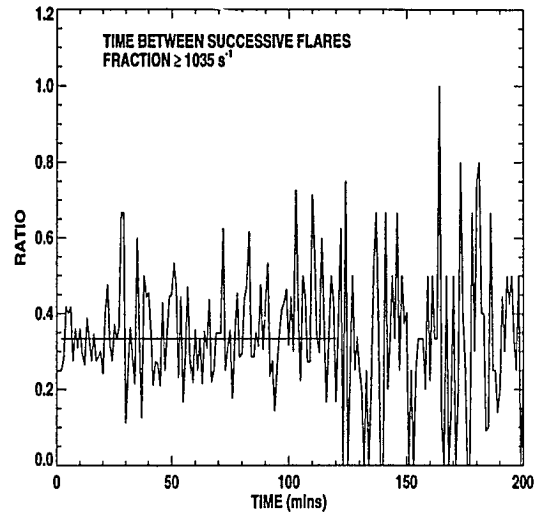


Fig. 5.22b. The percentage of flares with peak rates $\geq 1035 \text{ s}^{-1}$ as a function of time after the occurrence of the flare until the next flare. We expect $1/3$ of the flares in each bin to be $\geq 1035 \text{ s}^{-1}$ and the fit to the data confirms that.

CHAPTER VI

DISCUSSION

In this chapter we consider how the results obtained in the previous chapter fit in to current physical models of the Sun and solar flares. We begin with the idea that solar flares could provide the necessary energy to heat the solar corona. Next, we consider two flare occurrence models: the 'avalanche' model of solar flares and a stochastic model. We then consider the possible mechanisms for triggering sympathetic flares. We also consider the question of solar periods and conclude with some comments on the time scales of solar activity.

Coronal Heating

The total energy losses in the corona have been estimated to be $\sim 10^{28}$ ergs s^{-1} for coronal holes and quiet regions and $\sim 10^{29}$ ergs s^{-1} for active regions (Withbroe and Noyes, 1977). The energy loss mechanisms are radiation, conduction, and mass flow. Many mechanisms have been proposed as the source of energy to replenish the losses and maintain the million degree corona, however, it is difficult to find any mechanism capable of dissipating the required power. Because solar magnetic fields are ubiquitous and contain large amounts of energy, it has been suggested that magnetic reconnection events could provide the necessary energy (Gold, 1964; Tucker, 1973; Levine, 1974; Parker, 1983). Since solar flares are a manifestation of magnetic reconnection, they are a likely candidate for coronal heating.

Observations of flares have thus far shown that there is not enough energy released in solar flares to account for coronal heating. The total energy in accelerated elec-

trons in the flare frequency distribution obtained in the first UC–Berkeley balloon experiment (Fig 3.2) was found to be 10^{24} ergs s^{-1} for a non-thermal, thick target flare model (Lin *et al.*, 1984). In addition, the second flight of the instrument, during solar minimum, detected no flares (Lin *et al.*, 1991). The longest single interval of continuous solar observations during the second flight was ~ 5.5 hrs. One might expect that if flares are the source for coronal heating that the corona would cool during intervals when no flares occur.

We estimate a cooling time τ_c for the corona by assuming that the corona gas is a reservoir of particles with total energy (E_{th}) equal to the thermal content of the particles in the corona ($E_{th} = \int_{R_{\odot}}^{\infty} r^2 3kn(r)T(r)dr$). The density profile $n(r)$ is derived from observations and the temperature profile is derived for heat flow in a steady state atmosphere ($\nabla \cdot (\kappa \nabla T) = 0$). The thermal energy content of the coronal gas is estimated to be $\sim 2 \times 10^{32}$ ergs. The system, i.e. the corona, is in a steady-state, so the heat input as estimated by Withbroe and Noyes must equal the heat output ($P_{in} = P_{out}$). If the heat input is turned off, then the heat in the corona will be depleted in a time

$$\tau_c = \frac{E_{th}}{P_{out}} \approx 10^4 \text{ s.} \quad (6.1)$$

This cooling time τ_c is approximately equivalent to the length of time that Lin *et al.* detected no flares. Unless such intervals are extremely rare, flares with peak fluxes greater than 10^{-2} ph $cm^{-2} s^{-1} keV^{-1}$ cannot heat the corona, as the corona is never observed to cool significantly.

This does not rule out the possibility that flares with fluxes smaller than those observed by Lin *et al.* could heat the corona. It has been suggested that photospheric motions shuffling the coronal magnetic fields could cause reconnection to occur when the angle between a magnetic flux bundle and the mean field direction exceeds 14° (Parker, 1988). The energy comes from the work that the photospheric motions do in stressing the magnetic fields. The energy released in a typical reconnection event

is estimated to be 10^{24} ergs. This is ~ 3 orders of magnitude smaller than the Lin *et al.* microflares, so these reconnection events are termed *nanoflares* by Parker (1988).

It has been shown that if the flare size frequency distribution power-law index remains constant, even down to the nanoflare size, then there is not enough energy in solar flares to heat the corona (Hudson, 1991). The BATSE instrument cannot observe flares smaller than those observed by Lin *et al.* However, if the flare size frequency distribution slope steepens for flares smaller than the BATSE threshold, then flares could provide the necessary energy and we can search for evidence of a steeper slope in the BATSE frequency distribution.

The size frequency distribution of solar flares has been shown to be a power-law when plotted in terms of many kinds of measurements (Table 6.1). Thus, following the work of Hudson (1991), the distribution may be written as

$$\frac{dn}{dW_r} = AW_r^{-\alpha}, \text{ where} \quad (6.2)$$

$W_r \equiv$ total radiated flare energy. The total power (P) in the flare frequency distribution is calculated by integrating the distribution over sizes from the smallest flares to the largest flares observed

$$P = \int_{W_{r_{\min}}}^{W_{r_{\max}}} \frac{dn}{dW_r} W_r dW_r = \frac{A}{2-\alpha} [W_{r_{\max}}^{2-\alpha} - W_{r_{\min}}^{2-\alpha}]. \quad (6.3)$$

It is clear that for power-law indices $|\alpha| < 2$ the power in the distribution depends on the largest flares. For $|\alpha| > 2$, the small flares contribute the most power. Hudson estimates that the currently observed flare frequency distributions provide only about 2×10^{25} ergs s^{-1} in radiated flare energy, so large flares do not provide enough energy for coronal heating. The only way flares can be responsible for coronal heating is if the small flare frequency distribution obeys a steeper power-law index.

Flare frequency distributions are generally plotted in terms of quantities such as flare peak count rate (C), as was done in this work, or flare peak flux. In order to determine if the same critical slope dependence, $|\alpha| = 2$, is relevant to the distributions

SOLAR FLARE FREQUENCY SIZE DISTRIBUTIONS							
Author	Experiment	Dates	Observable	Energy	Measurement	Index	
Dennis (1985)	OSO V	1969 - 1971	Hard X-rays			-1.9	
Datlowe <i>et al.</i> (1974)	OSO VII	10/71 - 6/72	Hard X-rays	10 - 300 keV	Peak Flux@20 keV $ph (cm^2 s keV)^{-1}$	-1.8	
Lin <i>et al.</i> (1984)	Balloon	6/27/80	Hard X-rays	13 - 600 keV	Peak Flux@20 keV $ph (cm^2 s keV)^{-1}$	-2	
Dennis (1985)	HXRBS	2/80 - 2/85	Hard X-rays	30 - 500 keV	Peak Rate $cts s^{-1}$	-1.8	
Kurt (1990)	VENERA 13, 14	1981 - 1983	Hard X-rays	70 - 350 keV	Fluence	-1.45 ± 0.15	
Schwartz <i>et al.</i> (1992)	BATSE	4/91 - 9/91	Hard X-rays	25 - 1900 keV	Peak Rate $cts (s 70cm^2)^{-1}$	-1.614 ± 0.030	
Schwartz <i>et al.</i> (1992)	HXRBS	2/80 - 11/89	Hard X-rays	30 - 500 keV	Peak Rate $cts (s 70cm^2)^{-1}$	-1.729 ± 0.009	
Schwartz <i>et al.</i> (1992)	HXRBS	2/80 - 12/86	Hard X-rays	30 - 500 keV	Peak Rate $cts (s 70cm^2)^{-1}$	-1.754 ± 0.011	
Schwartz <i>et al.</i> (1992)	HXRBS	1/87 - 11/89	Hard X-rays	30 - 500 keV	Peak Rate $cts (s 70cm^2)^{-1}$	-1.657 ± 0.018	
Crosby <i>et al.</i> (1993)	HXRBS	1980 - 1982	Hard X-rays	30 - 500 keV	Peak Rate $cts s^{-1}$	-1.73 ± 0.01	
Crosby <i>et al.</i> (1993)	HXRBS	1983 - 1984	Hard X-rays	30 - 500 keV	Peak Rate $cts s^{-1}$	-1.71 ± 0.04	
Crosby <i>et al.</i> (1993)	HXRBS	1985 - 1987	Hard X-rays	30 - 500 keV	Peak Rate $cts s^{-1}$	-1.68 ± 0.07	
Crosby <i>et al.</i> (1993)	HXRBS	1988 - 1989	Hard X-rays	30 - 500 keV	Peak Rate $cts s^{-1}$	-1.67 ± 0.03	
Bai (1993)	HXRBS	1980 - 1981	Hard X-rays	30 - 500 keV	Peak Rate $cts s^{-1}$	-1.79 ± 0.02	
Bai (1993)	HXRBS	1982 - 1984	Hard X-rays	30 - 500 keV	Peak Rate $cts s^{-1}$	-1.72 ± 0.03	

SOLAR FLARE FREQUENCY SIZE DISTRIBUTIONS <i>continued</i>							
Author	Experiment	Dates	Observable	Energy	Measurement	Index	
Bai (1993)	HXRBS	1980 - 1983	Hard X-rays	30 - 500 keV	Peak Rate $cts\ s^{-1}$	-1.86 ± 0.03 ¹	
Bai (1993)	HXRBS	1980 - 1983	Hard X-rays	30 - 500 keV	Peak Rate $cts\ s^{-1}$	-1.70 ± 0.03 ²	
Aschwanden <i>et al.</i> submitted	HXRBS		Hard X-rays	50 - 100 keV	Peak Rate $cts\ s^{-1}$	-1.8 ³	
Drake <i>et al.</i> (1971)	Explorer 33, 35	7/66 - 9/68	Soft X-rays	1 - 6 keV	Peak Flux $ergs\ (cm^2\ s)^{-1}$	-1.75 ± 0.1	
Hudson <i>et al.</i> (1969)	OSO III	3/67	Soft X-rays	7.7 - 12.5 keV	Peak Rate $cts\ (cm^2\ s)^{-1}$	-1.8 ⁴	
Shimizu (1994)	YOHKOH SXT	8/15-20/92	Soft X-rays	6563 Å	Energy $ergs$	$-1.5 - -1.6$	
Fitzenreiter <i>et al.</i> (1976)	IMP VI	5/71 - 7/71	Radio Type III Burst	110 - 4900 kHz	Peak Flux $w\ (m^2\ Hz)^{-1}$	$-1.2 - -1.7$ ⁵	
Akabane (1956)	Ottawa, Tokyo Toyokawa	1/51 - 9/56	μ -waves	3000 MHz	Peak Flux $w\ (m^2\ Hz)^{-1}$	-1.8 ⁶	
Kakinuma <i>et al.</i> (1969)	Toyokawa	7/57 - 12/62	μ -waves	1000, 2000, 3750 and 9400 MHz	Peak Flux $w\ (m^2\ Hz)^{-1}$	-1.8 ⁷	
Kakinuma <i>et al.</i> (1969)	Toyokawa	7/57 - 12/62	μ -waves	3750 and 9400 MHz	Peak Flux $w\ (m^2\ Hz)^{-1}$	$-1.9 - -2.5$ ⁸	
Kundu (1965)		1958 - 1959	μ -waves	³ cm 10.7 cm	Peak Flux $w\ (m^2\ Hz)^{-1}$	-1.5 -1.5	

¹ Data from minimum phase of 153.8^d period.

² Data from maximum phase of 153.8^d period.

³ 5000 Hard X-ray pulses from 640 flares with 64 ms time resolution.

⁴ Slope estimated from distribution plotted by Hudson *et al.* (1969).

⁵ The power-law index was found to vary systematically over 10 observed frequencies.

⁶ Flares ≥ 5 s.f.u. Power-law independent of source distance from Central Meridian Passage.

⁷ Power-law independent of source position on solar disk. Power-law dependent upon polarization.

⁸ Power-law independent of source longitude.

SOLAR FLARE FREQUENCY SIZE DISTRIBUTIONS <i>continued</i>						
Author	Experiment	Dates	Observable	Energy	Measurement	Index
Kurochka (1987)	Various optical observatories	1978 - 1979	H α	6563 Å	Energy <i>ergs</i>	-1.77
Cliver <i>et al.</i> (1991)	IMP VIII	1977 - 1983	Protons	24 - 43 MeV	Peak Flux p ($cm^2 s sr MeV$) ⁻¹	-1.13 \pm 0.04
van Hollebeke <i>et al.</i> (1975)	IMP IV, V	5/67 - 12/72	Protons	20 - 80 MeV	Peak Flux@40 MeV p ($cm^2 s sr MeV$) ⁻¹	-1.15 \pm 0.1
Cliver <i>et al.</i> (1991)	IMP VIII	1977 - 1983	Electrons	3.6 - 18.5 MeV	Peak Flux e^- ($cm^2 s sr MeV$) ⁻¹	-1.30 \pm 0.07

Table 6.1. Solar flare size frequency distributions.

as generally plotted, we consider the relationship between flare energy and flare peak count rate. It was found that for flares detected with the SMM/HXRBS instrument the energy in flare accelerated electrons (W_{e-}), assuming a non-thermal, thick target model goes as $W_{e-} \sim C^{1.25}$ (Crosby *et al.*, 1993). This makes it even less likely that small flares heat the corona, as they are disproportionately less energetic. Calculating the power (P_{e-}) in the flare size frequency distribution as a function of flare peak count rate we find

$$P_{e-} = \int_{C_{min}}^{C_{max}} \frac{dn}{dC} W_{e-} dC \propto \frac{1}{2.25 - \gamma} [C_{max}^{2.25-\gamma} - C_{min}^{2.25-\gamma}] , \text{ where} \quad (6.4)$$

$$\frac{dn}{dC} \propto C^{-\gamma} . \quad (6.5)$$

Thus, the distribution of small flares, when plotted against peak rate, must have $|\gamma| > 2.25$ to be a significant source of coronal heating.

The flares detected with BATSE in this work extend the flare frequency distribution to flare sizes as small as $\sim 0.06 \text{ cm}^{-2} \text{ s}^{-1} \text{ keV}^{-1}$, for the peak flux at 20 keV. This is an order of magnitude smaller than previous long-term experiments and overlaps with the Lin *et al.* distribution. However, the Lin *et al.* distribution was plotted from only 25 events. We find that the flare size frequency distribution fits a constant power-law index of -1.68 , inconsistent with coronal heating by solar flares.

There are several assumptions which go into all of these calculations of energy available for coronal heating and which could change the results given here. There is an assumption that the energy available for coronal heating scales linearly with and is approximately equal to the energy that goes into accelerating electrons. We also assume that the photon energy spectrum of small solar flares is the same as large solar flares. Lastly, we assume a threshold energy for electron acceleration below which electrons are not accelerated. Changes in any of these assumptions could change our basic result that flares do not heat the corona.

While the total flare distribution, averaged over long times, cannot provide a significant amount of energy for coronal heating, there is a possibility that the flare

STELLAR FLARE FREQUENCY SIZE DISTRIBUTIONS						
Author	Source	Dates	Observable	Wavelength	Measurement	Index
Gershberg (1972)	UV Cet YZ CMi AD Leo EV Lac	1968 - 1971	B-band	4400 Å	B band Energy <i>ergs</i>	-1.91 ± 0.04 -1.50 ± 0.03 -1.38 ± 0.02 -1.66 ± 0.02
Lacy <i>et al.</i> (1976)	UV Cet YZ CMi AD Leo EV Lac CN Leo EQ Peg YY Gem Wolf 424 AB	1971 - 1972	U-band	3650 Å	Energy <i>ergs</i>	-1.98 ± 0.14 -1.71 ± 0.08 -1.82 ± 0.27 -1.69 ± 0.11 -1.99 ± 0.12 -2.00 ± 0.14 -1.43 ± 0.11 -1.81 ± 0.18
Gershberg <i>et al.</i> (1983)	23 Flare Stars		B-band U-band	4400 Å 3650 Å	bandpass Energy <i>ergs</i>	-1.49 -- -2.10 -1.32 -- -2.43
Petterson <i>et al.</i> (1984)	AD Leo	11/74 2/79 - 4/79 4/79 - 5/79 10/79 - 1/80	U-band	3650 Å	U band Energy <i>ergs</i>	-1.52 ± 0.13 -1.55 ± 0.12 -1.42 ± 0.10 -1.60 ± 0.13
Collura <i>et al.</i> (1988)	13 dMe Stars	1984 - 1985	X-rays	0.04 - 2keV	Energy <i>ergs</i>	-1.52
Ishida <i>et al.</i> (1991)	YZ CMi AD Leo EV Lac	1971 - 1988	U-band	3650 Å	U band Energy <i>ergs</i>	-1.56 ± 0.10 -1.47 ± 0.05 -1.52 ± 0.08

Table 6.2. Flare size frequency distributions for stellar sources.

size distribution is occasionally steep enough to heat the corona for short intervals. Variations have been found in the power-law index of flare size frequency distributions for flares from the Sun and from flare stars (Tables 6.1 and 6.2). There is evidence that the size distribution of flares detected with the SMM/HXRBS instrument show significant variations in the power-law index (variations of the order 0.1). Bai (1993) found variations with the phase of a 154 day period and the solar cycle. Crosby *et al.* (1993) found variations in the power-law index from year to year in the HXRBS data and evidence for a variation with the solar cycle. However, none of the reported variations cause the power-law index to be steep enough to be important for coronal heating. For stellar sources, there are large variations in the power-law index from star to star as well as variations in the index with time for individual stars. Due to their distance, stellar flare observations are limited to only very large flares. It is not clear how stellar flares are related to solar flares, but the variations in the power-law indices give reason to test solar flares for similar variations.

The only potentially significant variation in the power-law index obtained for BATSE observations was with the phase of a 51 day period in the flare occurrence rate. However, the steepest slope was only $\gamma = -1.74 \pm 0.04$, not nearly steep enough to account for coronal heating. When the data are plotted on shorter time scales (*e.g.* 25.5 days), the power-law index does vary more, but it is not statistically significant. Still, BATSE observations of flares provide no evidence for slopes steep enough to account for coronal heating.

Deviations From a Power-law Distribution

There are two data points, in the range between 100 s^{-1} and 200 s^{-1} , that deviate significantly from the power-law fit to the flare size frequency distribution (Fig. 5.1). These appear as excess counts just before the distribution turns over. These data seem to show that there is a steepening in the power-law below 200 s^{-1} . However, we believe that this steepening is not due to a relative increase in the number of flares at

these peak rates. We first note that the increase, while it is statistically significant, only equals 20% of the number of events in each interval. We find that all of the data points show similar deviations from the power-law when the deviation is plotted as a function of the number of events. Also, the differential distribution plotted for flares that occur during ideal observing conditions (Fig. 5.4) does not show the steepening in the range between 100 s^{-1} and 200 s^{-1} .

Possible reasons for the excess counts will be investigated in future work. It is possible that the deviations are real and that these data points, as well as others, are just a result of the data not really obeying a pure power-law. Another reason may be that variations in the detection efficiency (duty cycle and solar viewing angle) and the 51-day period in flare occurrence rate conspire to produce the effect (We have shown that there are small changes in the power-law index with the phase of the 51-day period.) Therefore, we conclude that a power-law describes (to $\sim 20\%$ precision) the full measurable range of flare sizes.

Avalanche Model of Solar Flares

In an effort to understand the observed flare size frequency distributions, Lu and Hamilton (1991) and Lu *et al.* (1993) developed an ‘avalanche’ model of solar flares. The model makes predictions about solar flare occurrence which can be tested with data from the BATSE instrument: (1) The power-law indices of the flare frequency distributions will be found to be independent of flare activity, and the same in different active regions, and (2) No significant correlation is expected between the energy of a flare and the time interval until the next flare or between the energy of a flare and the time since the previous flare.

The solar flare avalanche model is based on the concept of self-organized criticality (Bak *et al.*, 1987, 1988). Self-organized critical systems are systems with many temporal and spatial degrees of freedom which naturally evolve to a critical state in which a minor event starts a chain reaction that can affect any number of elements

in the system (Bak and Chen, 1991).

The paradigm for avalanche theory is the reaction of a sandpile as individual sand grains are added to it. As grains are dropped the sandpile grows in height with the slope of the pile increasing until reaching some steady state value. As more grains of sand are added, the sandpile slope stays constant through redistributions of the sand. When a grain of sand that lands on the pile causes the local slope to exceed some critical value an avalanche occurs. The avalanche continues if the initial movement causes neighboring sites to exceed their critical slope. The size of an avalanche can be measured by the number of grains of sand that fall off the pile. Most times only a few grains of sand fall. Much less often, large avalanches occur but the number of sand grains in even the largest avalanches is always much less than the total number of grains in the pile. The distribution of avalanches is described by a power-law in the avalanche size. The power-law index is robust and is independent of the sandpile slope. Of particular note is that the average sandpile slope is constant, even after the largest avalanches, so the system is always in a critical state ready to produce avalanches of all sizes. In this critical state, the system consists of many minimally stable regions of all sizes which are separated by enough to prevent the propagation of noise from one region to the next. Thus, the system has no length or time scales and this results in the power-law distributions.

The solar flare version of the avalanche model is a 3-dimensional grid of points where a magnetic field vector (\vec{B}_i) is defined at each point (i) on the grid (Lu and Hamilton, 1991; Lu *et al.*, 1993). In a manner analogous to dropping sand onto a sandpile, perturbations of magnetic field ($\delta\vec{B}_i$) are distributed at random locations on the grid. When the gradient of \vec{B}_i ($|\text{d}\vec{B}_i|$) exceeds some critical value (B_c), a fraction of the \vec{B}_i is redistributed among the nearest neighbor sites, i.e. a flare occurs. The gradient is defined as

$$\text{d}\vec{B}_i = \vec{B}_i - \sum_j \omega_j \vec{B}_{i+j} , \quad (6.6)$$

and the redistribution of \vec{B}_i is determined by

$$\vec{B}_i \rightarrow \vec{B}_i + \vec{b}_0 \quad \text{and} \quad (6.7a)$$

$$\vec{B}_{i+j} \rightarrow \vec{B}_{i+j} + \vec{b}_j, \quad (6.7b)$$

where \vec{b}_j is the field vector transported in the j direction. The instability criterion ω_j and the redistribution \vec{b}_j can be adjusted to simulate different conditions. If the gradient of \vec{B} at the neighboring sites then exceeds the critical value, the redistribution, or flare continues. The flare ends when there are no more sites exceeding the critical gradient. Each flare can be characterized by the number of steps in which at least one reconnection occurs (duration), the total number of redistributions (energy), and the maximum number of redistributions occurring at one time (peak rate). The rate of flaring corresponds to the rate at which magnetic field is deposited. The frequency distributions in each of these parameters conforms to a power-law. They find a flare peak flux (P) distribution of $N(P) \propto P^{-1.8}$. The power-law index is insensitive to the size of the 3-dimensional grid and to the magnitude of the instability criteria. However, variations in the power-law index occur if the instability criteria (ω_j) has a preferred direction. Likewise, the power-law index changes if there is a preferred direction for the redistribution of magnetic field (\vec{b}_j).

Lu and Hamilton (1991) suggest that the instability criteria could be equivalent to the reconnection criterion proposed by Parker (1988). Whatever the instability criterion is, it must only be a function of the instantaneous field configuration.

Avalanche Model Predictions

Power-law index. One of the predictions of the avalanche model is that the power-law index of the flare frequency distribution is independent of flare activity, and the same in different active regions (Lu *et al.*, 1993). We may see evidence of variation in the power-law index of the BATSE flare frequency in only one case, the 51 day period in the flare occurrence rate (There is a 50% probability that the variation can

be explained by random chance). There are no other indications from BATSE flares that the power-law index changes with activity levels.

However, as discussed earlier, there are results that indicate the solar flare frequency distribution power-law changes (Bai, 1993; Crosby *et al.*, 1993). In addition, there are a wide range of power-law indices measured for the distributions of flares from star to star, as measured at optical wavelengths, and the power-law index varies on some stars (Table 6.2). Certainly, the avalanche model currently requires some changes if it is to describe stellar flare distributions, and any desirable solar flare model should be applicable to flares observed on other stars. It may also be necessary to modify the model to account for the suggested variations in the solar flare frequency distribution.

Ways to account for variations in the power-law index are offered by Lu *et al.* (1993). It was shown that the power-law index is sensitive to an instability criterion that is anisotropic with a preferred direction and to a method of redistributing magnetic field that is anisotropic. It is conceivable that an anisotropic effect exists for flaring in one active region. However, it is difficult to imagine how such changes could vary globally, thereby changing the power-law index.

Random occurrence of flares. The other prediction of the avalanche model that can be addressed is that there should be no appreciable correlation between the energy of a flare and the time interval until the occurrence of another flare or between the energy of a flare and the time elapsed since the previous flare (Lu *et al.*, 1993). This is a direct result of the nature of self-organized criticality in which the systems are always in a critical (or meta-stable) state, ready to release energy in an event of any size.

The BATSE data show that there is a $< 1\%$ probability that the time between two consecutive flares depends on the size of the first flare, thus agreeing with the avalanche model prediction. We would expect to see a correlation if large flares deplete

significant amounts of the free energy available for flares. The region would need time to recover to be able to produce more large flares. If there is some dependence on time between consecutive flares in a single active region, multiple active regions producing flares may mask that dependence. There is no identification of the BATSE flares from individual active regions. Usually, except for times of very high activity, there is only one active region producing flares. Even during periods of high activity, there is still usually only one active region responsible for a large fraction of all flares. For example, in early June, 1991 (TJDs 8409 to 8423) the active region NOAA #6659 produced the majority for 7 days. Also, as with all flare observations, the BATSE data are an incomplete sample. There is no way of knowing when smaller, undetected flares occur. However, the total energy in small flares is expected to be insignificant, as discussed earlier.

Stochastic Flare Model

Observations of solar and stellar flares led Rosner and Vaiana (1978) to develop a model that explains the power-law behavior found in the flare frequency distribution from both sources. We call this the stochastic flare model. We note that stellar flare distributions show a power-law behavior only for flares with large total energies, whereas for smaller flares the number of flares observed is less than that expected from an extrapolation of the power-law. The observed frequency distribution for small flares from stellar sources is consistent with flares being equally uniformly distributed in size (*i.e.* a flat distribution).

The stochastic model of Rosner and Vaiana (1978) assumes that the rate is described by a Poisson process with mean flare rate ν . This follows from other assumptions: (1) flaring is a stochastic process which effectively ‘destroys’ the configuration which leads to the flare (the system is in its ground state after the flare), (2) distinct flaring regions are physically uncoupled, and (3) the flare duration is much less than the mean time between successive flares.

These assumptions are not contradicted by the BATSE data. We have shown that there is no evidence for sympathetic flaring; *i.e.*, there is no correlation between the occurrence times of solar flares. There is only a 93% probability that the time of occurrence of flares is described by a random process. Also, during the most active days the mean time between flares is ~ 15 minutes. Although we do not measure flare duration in this experiment, the vast majority of flares have durations of a few minutes or less, so the assumption that flare duration is much less than the time between flares seems to be valid.

Given a Poisson distribution of flare times, the goal is to reproduce the observed power-law dependence of the flare size frequency distributions. Rosner and Vaiana showed that the power-law behavior can be explained by a process where the energy to be released in a flare is accumulated at a rate proportional to the total energy of the flaring region,

$$E(t) = E_0(e^{\alpha t} - 1) , \text{ where} \quad (6.8)$$

$E(t)$ is the free energy added to the flaring region, E_0 is the ground-state energy, and α is the rate at which the system is stressed. The resulting flare frequency distribution can be written as

$$\omega \propto \left(1 + \frac{E}{E_0}\right)^{-\gamma} , \text{ where} \quad (6.9)$$

ω is the flare frequency as a function of flare energy and

$$\gamma = \frac{(\nu + \alpha)}{\alpha} . \quad (6.10)$$

The observed solar flare frequency distribution is reproduced when E greatly exceeds the ground-state energy E_0 . The constant value for the flare frequency distribution of stellar flares is reproduced in the limit that $E/E_0 \rightarrow 0$, the total energy of a small stellar flare is less than the system ground-state energy.

The BATSE data do show a power-law behavior in the flare frequency distribution. However, the requirement of exponential energy buildup says that the longer the time

is between flares, the larger the second flare should be. This is not observed. As described earlier, there is a $< 1\%$ probability that the time between flares depends on flare size.

Also, the relative constancy of the power-law index implies that γ (Eq 6.10), is a constant. Thus, the mean flare rate ν and the rate of energy buildup α must conspire to keep the power-law slope constant, *i.e.*

$$\nu = (\gamma - 1)\alpha . \quad (6.11)$$

Eq. 6.11 is true for only one active region, but as described above, there is typically only one or two flare producing regions active at any time.

Crosby *et al.* (1993) concluded that α is constant throughout the solar cycle. They found that the HXRBS flaring rate varied by a factor of ~ 20 over the solar cycle and the sunspot number typically varies by a factor of 10–20, so they presumed the HXRBS average flare rate variation to be a result of the variation in sunspot number. However, there are large differences between active regions in the production of flares. Also, incomplete sampling of solar flares, due to missing small flares, may have resulted in the similarity of the two numbers. We believe that the Crosby *et al.* conclusion is incorrect, mostly because we measure only small variations in the power-law index over wide ranges of solar activity. The number of flares in each 27 day interval of Fig 5.9a vary by a factor of about 10, but the power-law index only varies by a factor of about 25%.

Sympathetic Flares

Evidence that particles can propagate from one flare site and trigger a flare elsewhere on the Sun has been observed (Simnett, 1974; Strong, 1994). Others have seen evidence that waves generated at one flare site can trigger flares elsewhere (Smith and Harvey, 1971; Gergeley and Erickson, 1975). Anecdotal evidence shows that sympathetic flares occur. We consider here the cases in which BATSE is capable of observing sympathetic flares and the results of the search for sympathetic flares.

We need to consider the distances over which flare disturbances will propagate on the time scales in this study. The automated flare search algorithm has a 2 minute interval following the detection of a flare in which another flare cannot be detected. Thus, any disturbance which travels so quickly that any possible observable effects would be over in 2 minutes cannot be investigated here. The maximum time interval that we look for sympathetic flaring is 2 hours. This turns out to be long enough that even the most slowly propagating disturbances will have traveled large distances across the Sun. We assume in the following discussion that an active region is typically $\lesssim 10^\circ$ in heliocentric angle in extent, though large active regions can be much larger. The distances between active regions is typically $\gg 10^\circ$.

An example of a fast moving disturbance would be energetic electrons. Even a relatively low energy electron (20 keV) travels 10^7 km ($15R_\odot$) in 2 minutes. Thus, there is no chance that we can observe sympathetic flares triggered by energetic electrons. However, if the triggering is caused by protons there is a good chance that the sympathetic flare could be observed with BATSE. Particles are constrained to follow magnetic field lines so they must travel paths that are much longer than the great-circle distance between two points. We take a typical distance that a particle must travel between two points on the Sun to be $2R_\odot$. Protons with energies < 700 keV will travel that distance in greater than 2 minutes.

Another likely trigger mechanism is flare associated waves. There are two wave types to consider; Alfvén waves and magnetoacoustic waves. Shear Alfvén waves propagate along magnetic field lines at the Alfvén velocity

$$V_A = \frac{B}{\sqrt{\mu\rho}} \approx 1000\text{--}3000 \text{ km s}^{-1} \text{ in the quiet and active regions, where} \quad (6.12)$$

B is the magnetic field strength, μ is the magnetic permeability, and ρ is density. Compressional Alfvén waves propagate perpendicular to the magnetic field at the Alfvén velocity. The other types of waves to consider are slow and fast magnetoacoustic waves, as classified by the phase speed, and only fast waves (or shocks) can

propagate across magnetic fields. The velocity of propagation across magnetic fields for a perpendicular shock is given by $V_f > \sqrt{c_s^2 + V_A^2} \approx 1000 \text{ km s}^{-1}$, where c_s is the sound speed. Fast shocks are the most common type seen on the Sun and they have been observed at speeds up to $\sim 1500 \text{ km s}^{-1}$. Moreton waves, a type of fast shock, are seen as spherically expanding shock fronts propagating with typical speeds of $\sim 1000 \text{ km s}^{-1}$ (Uchida, 1974). They were first seen in $H\alpha$ as expanding circular rings on the solar disk. They are also seen in radio as type II bursts. Type II radio bursts are associated with flares and are the result of emission at the plasma frequency. The part of the Moreton wave propagating out through the solar atmosphere is responsible for the type II radio burst. Along magnetic field lines, slow shocks travel at a velocity $\gtrsim c_s$ but $\ll V_A$ and the fast shock travels faster than V_A . The sound speed in the corona is typically $> 200 \text{ km s}^{-1}$.

If we consider how far typical waves will propagate in the 2 minute time interval, we find that Alfvén waves might travel $3.6 \times 10^4 \text{ km}$, corresponding to a maximum angular distance on the Sun of 3° . It would take an Alfvén wave about an hour to travel 1/4 of the way around the Sun. Fast shocks moving at $\sim 1000 \text{ km s}^{-1}$ would cover at most 10° in 2 minutes and would travel 1/4 of the way around the Sun in 20 minutes.

The two minute time restriction in the data severely restricts the ability to detect sympathetic flare effects that might be occurring within single active regions. Only sympathetic flaring within an active region resulting from slow-mode waves can be observed with BATSE. There is a possibility of observing sympathetic flaring in very large active regions caused by Alfvén waves and fast shocks. For interactions between active regions, all of the trigger mechanisms suggested above could be tested with the BATSE data, with the exception of electrons and very energetic protons ($\gtrsim 1 \text{ MeV}$).

We see no evidence of sympathetic flaring on a time scale between 2 minutes and 2 hours. The simulations of sympathetic flaring indicate that sympathetic triggering

does not occur in the majority of flares. Sympathetic flares are the exception rather than the rule. There are still some mechanisms by which sympathetic flaring could occur that we cannot test for. If electrons or high energy protons (> 1 MeV) accelerated in one flare trigger a flare elsewhere on the Sun, the second flare would occur within 2 minutes and we would not detect it. We also would not see sympathetic flares that occur within the same active region if the trigger mechanism is a fast shock, except for very large active regions. We do rule out more slowly propagating waves like slow shocks as a mechanism for triggering many sympathetic flares even in the case of flares occurring in the same active region. We also rule out the possibility of any wave mode or low energy protons as the trigger mechanism for substantial numbers of sympathetic flares between active regions.

Solar Periods

The only long lasting, well observed solar period is the 11 year variation in the sunspot number and the flare rate. Many observers have searched for periods at a wide range of wavelengths and solar indices. There have been many reported observations of other periods, but the detections have been very weak or have not lasted for long intervals. Of particular interest here are periods observed in the solar flare rate.

A 154 day period was discovered during solar cycle 21 in the occurrence rate of ≥ 300 keV flares measured with the SMM Gamma-Ray Spectrometer from 1980–1983 (Rieger *et al.*, 1984). Subsequently, the same period was found for SMM/HXRBS flares observed in the 25–140 keV energy range for the 1980–1983 interval (Kiplinger *et al.*, 1984). Following these discoveries, many reports of ~ 154 day periods were made for microwave bursts, 10.7 cm radio flux, sunspot number, sunspot area, solar proton events, solar flare electron events, and $H\alpha$ indices for solar cycles 19, 20 and/or 21 (Bogart and Bai, 1985; Ichimoto *et al.*, 1985; Lean and Brueckner, 1989; Carbonell and Ballester, 1990; Gabriel *et al.*, 1990; Dröge *et al.*, 1990).

Bai and Sturrock (1991) claimed that there is a fundamental period ~ 25.5 days.

They showed evidence for periods of 51, 78, 104, and 129 days detected in a variety of solar activity measures, including the 10.7 cm radio flux, sunspot area, and the γ -ray flare rate. These, as well as the 154 day period, are sub-harmonics of the fundamental period.

For the current solar cycle (22), Bai (1992, 1994), reports evidence for 51 and 77 day periods. The 77 day period was seen between November 1988 and February 1990, but not after. The 51 day period was detected in the interval from May 1991 to November 1992 in GOES flares of X-ray class $\geq M3.0$. That interval includes the time span covered in this work.

We do see evidence for the 51 day period, though it is detected only for large flares. There is no evidence for the 25.5 day period. There is also no evidence for any of the other sub-harmonics of the fundamental period. That there is evidence for the 51 day period in large flares is not unexpected, as the period had already been observed in large flares at other wavelengths. What is surprising is the apparent size threshold required to detect the period. This threshold may account for why the period is hard to detect, as there are comparatively few large events and there are frequently long intervals with none.

This threshold effect may also account for the hint of a variation found in the power-law index of the flare size frequency distribution. For the power-law index to change, the relative number of large to small flares must change. The smaller (flatter) power-law index from the peak phase of the 51 day period indicates that large flares are preferred relative to small flares during that phase. Similar results have been found for the peak phase of the 154 day period (Bai, 1993). Also, preliminary results show the flare size distribution for flares from large, complex active regions is flatter than for flares from small, simple active regions (Kucera, 1994).

Since large flares are likely to come from large, complex active regions, these results are consistent. It appears that favorable conditions for large flares tend to

recur periodically. It also appears that complex regions tend to favor the production of large flares over small flares.

Bai and Sturrock (1987) considered the possibility that the 154 day period results from the interactions of complexes of activity or 'hot spots' found by Bai (1987). A similar mechanism was proposed by Ichimoto *et al.* (1985). The hot spots of Bai are intervals of Carrington longitude which produce many flares. Carrington longitudes are a coordinate system defined to rotate with the Sun, thus the 'hot spots' are locations on the Sun where flare activity recurs. Bai and Sturrock (1987) concluded that the 154 day period is not the result of 'hot spots' or the interaction of 'hot spots' due to differential rotation.

One proposed mechanism for short solar periods is based on gravity wave modes (g-modes). The normal modes of small amplitude oscillations caused by buoyancy are called g-modes and each mode has a spherical harmonic dependence (Cowling, 1941). It has been shown that interactions of these modes are enhanced in a rotating star and the 154 day period can be explained by interactions of rotating modes (Wolff, 1974a, 1974b, 1983). The interactions of the modes drive large-scale flows which cause enhancements in solar activity.

Whatever the mechanism by which the periods are created, the data show that it should create a relative enhancement in the rate of large flares.

Complexes of Activity 'Hot Spots'

As already mentioned, Bai (1987) has identified Carrington longitudes where active regions tend to reappear. New active regions tend to form where old active regions had been (Švestka, 1968; Bumba and Howard, 1965a, 1965b). Particular Carrington longitudes can be centers of activity for several years. There is evidence that some complexes of activity last for several solar cycles (Bai, 1988). There is not necessarily always an active region present in the complex, though.

There can be any number of activity complexes at one time and there are usually

more than one. During the previous solar cycle (cycle 21), two hot spots in the northern hemisphere, separated by 180° and one hot spot in the southern hemisphere were active (Bai, 1988). One of the northern hot spots has been active from solar cycle 19 to the start of solar cycle 22 and the other has persisted since cycle 20. The southern hemisphere hot spot has persisted since cycle 19 and there is evidence that another southern hot spot is emerging.

We find that flare activity persists for up to 32_{-8}^{+16} days, with little or no indication that the Sun continuously produces flares for intervals longer than this. If there were only one active hot spot then the longest we would expect to see continuous flare activity is about 14 days. Thus, there must be at least two hot spots producing flares from 1991 to 1992 separated so that one is always visible from earth. Also, Strong (1994) found the integrated flux variation in soft X-rays peaks for several weeks, implying that the activity is a global phenomenon rather than being a local phenomenon associated with single active regions. It is possible that these are the hot spots detected by Bai (1988) continuing to persist in the maximum phase of solar cycle 22. However, the data also suggest that the hot spots produce bursts of flares for only up to about one solar rotation at a time. The hot spots don't seem to be producing flares continuously.

The long term persistence of the hot spots would indicate that they are a feature of the magnetic dynamo. In fact, they must survive the switch of the magnetic poles every 22 years.

CHAPTER VII

CONCLUSIONS

This dissertation was an investigation of the properties of solar flares detected with the Burst and Transient Source Experiment. A comparison of the global properties of small flares to large flares was made to gain insight into flare occurrence and to determine the importance of small flares in coronal heating.

The differential frequency distribution of flare peak rates was fit with a single power-law in the event peak rate. The index was found to be -1.7 over a range of peak rates covering four orders of magnitude. The measured index rules out the small flares observed with BATSE as a significant source of coronal heating, as long as we can assume that the energy in accelerated electrons is representative of the energy available for heating and that estimates of the energy in electrons are correct. The single power-law index also indicates that there are no significant differences in the processes generating small and large flares. This suggests that small flares are useful for studies of the flaring process. It should be easier to isolate and understand the physical processes occurring during small flares because the physical conditions at the flare site are likely to be much more uniform than during large flares.

There is a 51 day period evident in the large flare occurrence rate that does not exist in the smaller flares. This size threshold for the period means that there are periodic intervals when the relative number of large flares to small flares increases, also evident as a 2σ change in the power-law index as a function of phase in the 51 day cycle (see below). Thus, there is some periodic favorable condition for large

flares that exists for active regions. There is no evidence for the 25.5 day fundamental period proposed by Bai and Sturrock (1991). There was also no indication of the 154 day period that was discovered in the previous solar cycle.

Variability in the power-law index of the differential frequency distribution of flare peak rates was found in only one case; with the phase of a 51 day period. The power-law index was found to be -1.65 ± 0.03 during the maximum phase of the period and -1.74 ± 0.04 during the minimum phase of the period. This is expected if there is a threshold effect in the size frequency distribution. This result corroborates earlier suggestions the size distribution flattens during certain phases of high activity (Bai, 1993; Kucera, 1994). However, the steepening of the slope for high activity may just be a result of small flares not being detected because they are occurring during the large flares. Long duration events with high count rates will make it difficult to detect small events until the large flare ends.

We found no other evidence that the power-law index of the frequency distribution of flare peak rates varies with activity levels. This was tested by measuring the power-law index as a function of the number of flares observed in intervals of constant length in time. It was also tested by subjectively dividing the flares into two groups, one of high activity, the other of low activity.

We found that sympathetic flaring is only allowed as a trigger mechanism for at most 25% of the flares, if the sympathetic flares occur between 2 and 40 minutes after the initial flare. Outside this interval, we cannot exclude any amount of sympathetic flaring. Our data are consistent with the times of occurrence of solar flares being described by a Poisson process with a slowly varying mean flare rate.

BATSE observations of flares were also used to test avalanche models of solar flares. In particular, two predictions of Lu *et al.* (1993) were tested: (1) that the power law indices of flare frequency distributions will be found to be independent of flare activity, and the same in different active regions, (2) no appreciable correlation

between the energy of a flare and the time interval until the occurrence of another flare or between the energy of a flare and the time elapsed since the previous flare is expected.

We found that there is no correlation between the size of flares and the time between successive flares. This indicates that during periods of flare activity, the system that generates flares is never far from its critical flare producing state, even after large flares. Thus, the observations of BATSE support the second prediction of the avalanche model for solar flares.

Although there was variability found in the power-law index of the flare frequency distribution, it was found in only one particular case and it was not a very significant variation (2σ). It is possible that the observed variation can be accounted for by the avalanche model in ways suggested by Lu *et al.* That is, to have an instability criterion or redistribution of magnetic energy which varies in a systematic way.

The results found here are inconsistent with the stochastic flare occurrence model of Rosner and Vaiana (1978). The model predicts that flares are Poisson distributed in time, which we confirm. However, the model also predicts a correlation between the size of flares and the time between successive flares, which we do not find.

We found that if sympathetic flaring is to be an important mechanism for flare occurrence then the sympathetic flare must occur very close to the original flare or be triggered by electrons or high energy (> 1 MeV) protons. The limiting cases are determined by the 2 minute interval between flares that the automated algorithm requires to prevent counting a flare more than once. Low energy protons and waves can only trigger a significant fraction of flares if the sympathetic flare occurs within about 3° of the initial flare. Electrons and high energy protons can travel far enough within 2 minutes to have initiated a flare at any point on the sun and these flares would have gone undetected.

Continued observations of solar flares with BATSE would prove to be useful for

several of the topics discussed. Certainly any search for periodic behavior in the flare occurrence rate would benefit from a longer time series. Also, if the 51 day period continues, the variation of the power-law index with the phase of the period may become more significant. Also, the data can be tested for differences in the power-law index detected during solar maximum and during solar minimum. The wavelet analysis used to look for structures of activity would also be improved with a longer data set. It is possible that the sympathetic flaring result could be more rigorously tested during solar minimum, when there is rarely more than one active region producing flares. It should be noted however, that as solar minimum is approached, the flare rates will drop dramatically.

Further observations will not change the basic result that the flares detected with BATSE cannot heat the corona. More data will only serve to reduce the errors in the power-law index, the slope will not change significantly.

LIST OF REFERENCES

- Akabane, K., *Publ. Astron. Soc. Japan*, **8**, No. 3-4, 173, 1956.
- Aschwanden, M.J., Schwartz, R.A., and Alt, D.M., *Ap. J.*, submitted.
- Athay, R.G., "The Solar Chromosphere and Corona: Quiet Sun", D. Reidel, Boston, 1976.
- Bai, T., *Ap. J.*, **314**, 795, 1987.
- Bai, T. and Sturrock, P.A., *Nature*, **357**, 601, 1987.
- Bai, T., *Ap. J.*, **328**, 860, 1988.
- Bai, T. and Sturrock, P.A., *Nature*, **350**, No. 6314, 141, 1991.
- Bai, T., *Ap. J.*, **388**, L69, 1992.
- Bai, T., *Ap. J.*, **404**, 805, 1993.
- Bai, T., *Solar Physics*, **150**, 385, 1994.
- Bak, P., Tang, C., and Wiesenfeld, K., *Phys. Rev. Letters*, **59**, No. 4, 381, 1987.
- Bak, P., Tang, C., and Wiesenfeld, K., *Phys. Rev. A*, **38**, No. 1, 364, 1988.
- Bak, P. and Chen, K., *Scientific American*, **46**, January, 1991.
- Bastian, T.S., *Ap. J.*, **370**, L49, 1991.
- Becker, U., *Z. Astrophys.*, **44**, 243, 1958.
- Bogart, R.S. and Bai, T., *Ap. J.*, **299**, L51, 1985.
- Brown, J.C., *Solar Physics*, **18**, 489, 1971.
- Bumba, V. and Howard, R., *Ap. J.*, **141**, 1492, 1965.
- Bumba, V. and Howard, R., *Ap. J.*, **141**, 1502, 1965.
- Canfield, R.C. and Metcalf, T.R., *Ap. J.*, **321**, 586, 1987.
- Carbonell, M. and Ballester, J.L., *Astron. Astrophys.*, **238**, 377, 1990.
- Chase, R.C., Krieger, A.S., Švestka, Z., and Vaiana, G.S., *Space Research*, **XVI**, 917, 1976.
- Cheng, C., Tandberg-Hanssen, E., and Orwig, L.E., *Ap. J.*, **278**, 853, 1984.
- Cliver, E., Reames, D., Kahler, S., and Cane, H., *Proc. 22nd ICRC, Dublin*, **3**, 25, 1991.
- Collura, A., Pasquini, L., and Schmitt, J.H.M.M., *Astron. Astrophys.*, **205**, 197, 1988.
- Cowling, T.G., *M.N.R.A.S.*, **101**, 347, 1941.

- Crosby, N.B., Aschwanden, M.J., and Dennis, B.R., *Solar Physics*, **143**, 275, 1993.
- Datlowe, D.W., Elcan, M.J., and Hudson, H.S., *Solar Physics*, **39**, 155, 1974.
- de Jager, C. and de Jonge, G., *Solar Physics*, **58**, 127, 1978.
- Dennis, B.R., *Solar Physics*, **100**, 465, 1985.
- Drake, J.F., *Solar Physics*, **16**, 152, 1971.
- Dröge, W., Gibbs, K., Grunsfeld, J.M., Meyer, P., Newport, B.J., Evenson, P., and Moses, D., *Ap. J. Suppl.*, **73**, 279, 1990.
- Fishman, G.J., Meegan, C.A., Wilson, R.B., Paciesas, W.S., Parnell, T.A., Austin, R.W., Rehage, J.R., Matteson, J.L., Teegarden, B.J., Cline, T.L., Schaefer, B.E., Pendleton, G.N., Berry, Jr., F.A., Horack, J.M., Storey, S.D., Brock, M.N., and Lestrade, J.P., "Proceedings of the Gamma Ray Observatory Science Workshop," 2-39, 1989.
- Fitzenreiter, R.J., Fainberg, J., and Bundy, R.B., *Solar Physics*, **46**, 465, 1976.
- Forrest, D.J. and Chupp, E.L., *Nature*, **305**, 291, 1983.
- Fritzová-Svestková, L. and Chase, R., *BAAS*, **7**, No. 3, 439, 1975.
- Gabriel, A., *Phil. Trans. Roy. Soc. London*, **281**, 339, 1976.
- Gabriel, S., Evans, R., and Feynman, J., *Solar Physics*, **128**, 415, 1990.
- Gergely, T.E. and Erickson, W.C., *Solar Physics*, **42**, 467, 1975.
- Gershberg, R.E., *Astrophys. and Space Sci.*, **19**, 75, 1972.
- Gershberg, R.E. and Shakhovskaya, N.I., *Astrophys. and Space Sci.*, **95**, 235, 1983.
- Gold, T. and Hoyle, F., *MNRAS*, **120**, No. 2, 1960.
- Gold, T., in 'The Physics of Solar Flares,' W. Hess (ed.), NASA SP-50, 389, 1964.
- Hudson, H.S., Peterson, L.E., and Schwartz, D.A., *Ap. J.*, **157**, 389, 1969.
- Hudson, H.S., *Solar Physics*, **133**, 357, 1991.
- Hunt, J.C.R., Kevlahan, N.K.-R., Vassilicos, J.C., and Farge, M., "Wavelets, Fractals, and Fourier Transforms," M. Farge, J.C.R. Hunt, and J.C. Vassilicos (ed.), Clarendon Press, 1, 1993.
- Ichimoto, K., Kubota, J., Suzuki, M., Tohmura, I., and Kurokawa, H., *Nature*, **316**, 422, 1985.
- Ishida, K., Mahasenaputra, Ichimura, K., and Shimizu, Y., *Astrophys. and Space Sci.*, **182**, 227, 1991.
- Kakinuma, T., Yamashita, T., and Enome, S., "Proceedings of the Research Institute

- of Atmospherics, Nagoya, University”, *16*, 127–141, 1969.
- Kiplinger, A.L., Dennis, B.R., and Orwig, L.E., *BAAS*, *16*, 891, 1984.
- Kniffen, D.A., “Proceedings of the Gamma Ray Observatory Science Workshop, Greenbelt MD,” 1-1, 1989.
- Krieger, A.S., Timothy, A.F., and Roelof, E.C., *Solar Physics*, *29*, 505, 1973.
- Kucera, T.A., *EOS Supplement*, *75*, 286, 1994.
- Kundu, M.R., “Solar Radio Astronomy,” Interscience Publishers, New York, p. 204, 1965.
- Kurochka, L.N., *Sov. Astron.*, *31*(2), 231, 1987.
- Kurt, V.G., *Basic Plasma Processes on the Sun*, eds. E.R. Priest and V. Krishan, 409, 1990.
- Lacy, C.H., Moffett, T.J., and Evans, D.S., *Ap. J. Suppl.*, *30*, 85, 1976.
- Lean, J.L. and Brueckner, G.E., *Ap. J.*, *337*, 568, 1989.
- Levine, R.H., *Ap. J.*, *190*, 457, 1974.
- Lin, R.P., Schwartz, R.A., Kane, S.R., Pelling, R.M., and Hurley, K.C., *Ap. J.*, *283*, 421, 1984.
- Lin, R.P., Hurley, K.C., Smith, D.M., and Pelling, R.M., *Solar Physics*, *135*, 57, 1991.
- Lu, E.T. and Hamilton, R.J., *Ap. J.*, *380*, L89, 1991.
- Lu, E.T., Hamilton, R.J., McTiernan, J.M., and Bromund, K.R., *Ap. J.*, *412*, 841, 1993.
- Mariscotti, M.A., *Nuclear Instruments and Methods*, *50*, 309, 1967.
- Neupert, W.M. and Pizzo, V., *JGR*, *79*, No. 25, 3701, 1974.
- Newland, D.E., “An introduction to Random vibrations, spectral and wavelet analysis.”, John Wiley and Sons, New York, 1993.
- Nolte, J.T., Krieger, A.S., Timothy, A.F., Gold, R.E., Roelof, E.C., Vaiana, G., Lazarus, A.J., Sullivan, J.D., and McIntosh, P.S., *Solar Physics*, *46*, 303, 1976.
- Orwig, L.E., Frost, K.J., and Dennis, B.R., *Solar Physics*, *65*, 25, 1980.
- Parker, E.N., *Ap. J.*, *174*, 499, 1972.
- Parker, E.N., *Ap. J.*, *244*, 631, 1981.
- Parker, E.N., *Ap. J.*, *244*, 644, 1981.
- Parker, E.N., *Ap. J.*, *264*, 642, 1983.

- Parker, E.N., *Ap. J.*, **330**, 474, 1988.
- Pendleton, G.N., Pacias, W.S., Lestrade, J.P., Fishman, G.J., Wilson, R.B., and Meegan, C.A., "Proceedings of the Gamma Ray Observatory Science Workshop, Greenbelt, MD," 4-547, 1989.
- Pettersen, B.R., Coleman, L.A., and Evans, D.S., *Ap. J. Suppl.*, **54**, 375, 1984.
- Poland, A.I., Orwig, L.E., Mariska, J.T., Nakatsuka, R., and Auer, L.H., *Ap. J.*, **280**, 457, 1984.
- Porter, J.G., Toomre, J., and Gebbie, K.B., *Ap. J.*, **283**, 879, 1984.
- Porter, J.G., Moore, R.L., Reichmann, E.J., Engvold, O., and Harvey, K.L., *Ap. J.*, **323**, 380, 1987.
- Priest, E.R., "Solar Magnetohydrodynamics", D. Reidel, Boston, 1982.
- Richardson, R.S., *Ann. Rept. Director Mt. Wilson Obs.*, **35**, 871, 1936.
- Richardson, R.S., *Ap. J.*, **114**, 356, 1951.
- Rieger, E., Share, G.H., Forrest, D.J., Kanbach, G., Reppin, C., and Chupp, E.L., *Nature*, **312**, 623, 1984.
- Rosner, R. and Vaiana, G.S., *Ap. J.*, **222**, 1104, 1978.
- Schwartz, R.A., Dennis, B.R., Fishman, G.J., Meegan, C.A., Wilson, R.B., and Pacias, W.S., NASA CP-3137, 457, 1992.
- Shimizu, T., "Proceedings of Kofu Symposium," NRO Report No. 360, 61, 1994.
- Smith, H.J. and Smith, E.v.P., "Solar Flares", The Macmillan Co., New York, 92, 1963.
- Smith, S.F. and Harvey, K.L., "Physics of the Solar Corona", C.J. Macris (ed.), 156, 1971.
- Simnett, G.M., *Solar Physics*, **34**, 377, 1974.
- Simnett, G.M. and Dennis, B.R., *Proc. of 19th ICRC*, **4**, 38, 1985.
- Strong, K., "Proceedings of Kofu Symposium," NRO Report No. 360, 53, 1994.
- Sturrock, P.A. and Bai, T., *Ap. J.*, **397**, 337, 1992.
- Švestka, Z., *Solar Phys.*, **4**, 18, 1968.
- Tucker, W.H., *Ap. J.*, **186**, 285, 1973.
- Uchida, Y., *Solar Phys.*, **39**, 431, 1974.
- van Beek, H.F., de Feiter, L.D., and de Jager, C., *Space Research*, **XIV**, 30, 1974.

van Hollebeke, M.A.I., Ma Sung, L.S., and McDonald, F.B., *Solar Physics*, 41, 189, 1975.

Waldmeier, M., *Z. Astrophys.*, 15, 299, 1938.

Withbroe, G.L. and Noyes, R.W., *Ann. Rev. Astron. Astrophys.*, 15, 363, 1977.

Wolff, C.L., *Ap. J.*, 193, 721, 1974.

Wolff, C.L., *Ap. J.*, 194, 489, 1974.

Wolff, C.L., *Ap. J.*, 264, 667, 1983.

“This research has made use of data obtained through the CGRO BATSE Solar Flare Data Archive maintained by the Solar Data Analysis Center at NASA-Goddard Space Flight Center and provided by the BATSE team headed by Dr. Gerald Fishman.”